FORTE Measurements of Global Lightning Altitudes

Michael Peterson[1]

[1]ISR-2, Los Alamos National Laboratory, Los Alamos, New Mexico

Corresponding author: Michael Peterson (mpeterson@lanl.gov), B241, P.O. Box 1663 Los Alamos, NM, 87545

Key Points:

- A joint RF / optical method for retrieving lightning altitude from previous studies has been applied to the full FORTE record
- While global FORTE events concentrate in the upper (positive) charge layer at ~10 km, sources are also found at lower altitudes
- Source altitude is shown to depend on location, land or ocean terrain, season, and time in the parent flash

LA-UR 21-32433

Abstract

While multiple lightning detection systems provide geographical locations of lightning events across the globe, robust lightning altitude measurements on a global scale have proven elusive. Space-based platforms have an advantageous viewing geometry over ground-based systems for making these measurements, but prior studies with the Fast On-orbit Recording of Transient Events (FORTE) satellite were limited to a few thousand events. In this study, we apply the same technique for calculating source altitude from the previous efforts to a large catalog of hundreds of thousands of global FORTE in-cloud lightning events that were coincident with flashes geolocated by its lightning imager between 1997 and 2003. We use this data to document global variations in lightning altitude.

As in previous studies, we find that FORTE primarily resolves sources from the upper (positive) charge layer at ~11 km altitude in normal thunderstorms. However, sources are also recorded from other charge layers in the storm, and from leaders developing between layers. In particular, we note a pronounced increase in source altitude in the first 20 ms of FORTE flashes from the negative leader developing upward into the upper positive charge layer. Regions known for wintertime and/or stratiform lightning have increased contributions from low-altitude sources, while tropical regions particularly around Panama and the Maritime Continent have the greatest concentrations of high-altitude sources.

Plain Language Summary

After many years of observing lightning from by multiple sensors, we have a good understanding of where lightning occurs in the world and how its frequency differs from region to region. However, the lightning that we witness on the ground (which is also the primary phenomenon detected by the global lightning networks) is only a small portion of the expansive lightning channels. Most of the flash extends through the clouds, hidden from view. The altitudes of lightning flashes in the clouds are particularly important because they reveal changes to convection and play a key role in atmospheric chemistry. In this study, we use a large global catalog of in-cloud lightning events recorded by the FORTE satellite to document lightning altitudes across the globe.

1 Introduction

The altitude of lightning within the cloud is controlled by the kinematics of the parent thunderstorm that organize charged precipitation particles into spatially-separated pockets with a surplus of either positive or negative charge. Under typical conditions in the Non-Inductive Charging (NIC) mechanism (Reynolds et al., 1957; Takahashi, 1978; Jayaratne et al., 1983; Saunders et a.l, 1991; Saunders & Peck, 1998; Takahashi & Miyawaki, 2002; Mansell et al., 2005), collisions between graupel rimed with supercooled liquid water and small ice particles in the thunderstorm updraft result in the heavier graupel attaining a negative charge and the lighter ice particles becoming positively charged. The updraft sorts these species of hydrometeors by mass, lofting the positively-charged ice particles towards the top of the cloud, while leaving the negatively-charged graupel in the mid-levels of the storm. This creates the main positive dipole (Wilson, 1920) that we see in the tripole structure of ordinary thunderstorms (Simpson and Scrase, 1937; summarized in Williams, 1989).

However, the diversity and complexity of thunderstorms leads to many different charge structures being observed that diverge substantially from this idealized tripole view. Some storms conflict with the tripole model entirely (i.e., Marshall and Rust, 1991), while others consist of a convective core with a primarily tripole structure adjacent to non-convective electrified clouds with their own unique charge structures. One notable example of a non-convective cloud with a distinct charge structure is the electrified anvil cloud. The upper positive layer extends laterally beyond the edge of the convective core into the overhanging anvil, and negative screening layers form on the upper and lower boundaries of the anvil cloud (Marshall et al., 1989). Additionally, electrified stratiform clouds are comprised of multiple vertically-confined yet horizontally-extensive layers of alternating positive and negative charge created by

in-situ electrification processes and the advection of charge from the convective core (Stolzeburg et al., 1998; Schuur and Rutledge, 2000; Ely et al., 2008; Lang and Rutledge, 2008). Thunderstorm charge structures also vary by season and location on Earth (summarized in Williams, 2018), with the inner tropics having particularly tall thunderstorms (López et al., 2019) and winter thunderstorms over the oceans surrounding Japan being well-known for their compact vertical extent (Yamamoto et al., 2006).

Because lightning flashes consist of positive and negative leaders that develop through these charge regions, it is possible to infer the charge structure of a given thunderstorm from the altitudes of lightning emissions sources. The key advantage of this approach over in-situ balloon soundings is that lightning source altitudes can be measured remotely at considerable distances using Radio-Frequency (RF) measurements. Lightning Mapping Arrays (LMAs: Rison et al., 1999) are networks of Very High Frequency (VHF) band RF receivers that are capable of mapping the three-dimensional structure of lightning flashes with a nominal accuracy of tens of meters (Thomas et al., 2004) and a maximum range on the order of a few hundred kilometers (depending on the number of stations in the array and their geometry). The locations of individual charge layers manifest as local maxima in the VHF source altitude profile, while the polarity of each layer can be inferred from the relative frequency of sources (Rison et al., 1999). This is possible because lightning processes associated with a negative leader propagating through a positive charge layer are more prevalent emitters of VHF radiation than positive leaders propagating through a negative charge layer. Manual techniques and, more recently, automated routines like chargepol (Medina et al., 2021), use VHF source altitudes to characterize the bulk thunderstorm charge structure.

In addition to informing thunderstorm charge structures, lightning altitude measurements

are also useful for revealing changes in updraft behavior (Suszcynsky and Heavner, 2003; Fierro et al., 2011) and quantifying the effects of lightning on atmospheric chemistry. Nitrogen oxides ($NO_x = NO+NO_2$) are a catalytic precursor in the photochemical production of tropospheric Ozone (O_3) (Crutzen, 1973; Chameides and Walker, 1973; Seiler and Crutzen, 1980; Crutzen et al., 1979), which is an important greenhouse gas in the upper troposphere (Fishman et al., 1979; Lacis e al., 1990). Numerous sources contribute to the NO_X budget including ground-level sources such as biomass and hydrocarbon burning, and atmospheric sources including aircraft emissions and lightning (LNO_x). Ivanov et al. (2014) identified the temperature threshold for NO_x production to occur as 3000-4000 K. The lightning leaders that can be mapped with VHF measurements like LMAs typically have temperatures around 10,000 K (Rakov et al., 2003). Thus, these leaders are an important source of LNO_x, and the LNO_x output from individual flashes is expected to be concentrated at the altitudes where the leaders propagate. Multiple lightning altitude profiles have been created from either lightning measurements or parameterizations that can be used to estimate the LNO_x mass distribution for regional and global chemical transport models (Pickering et al., 1998; DeCaria et al., 2000; Tie et al., 2002; Labrador et al., 2005; Luo et al., 2017; Carey et al., 2016; Mecikalski and Carey, 2018). However, none of these profiles are representative of global lightning. The parameterizations rely on many assumptions about how lightning altitude scales with environmental parameters, while the measured profiles were created from regional 3D lightning mapping systems (LMAs and others) that have limited ranges and only cover certain land-based regions of the Earth (which are heavily concentrated in the northern mid-latitudes).

Altitude profiles of VHF lightning sources are also available from space-based RF measurements. Jacobson et al. (1999) described a methodology for using the time delay between

122 the VHF pulses produced by the direct line-of-sight measurement of an in-cloud lightning source
123 and its reflection off the surface of the Earth to compute the altitude of the source above ground
124 level. This method requires that the position of the satellite and the geographic location of the
125 source be known. Light and Jacobson (2002) used this approach to generate VHF source altitude
126 distributions for FORTE events coincident with either the National Lightning Detection Network
127 (NLDN: Cummins et al., 1998) or FORTE's Optical Lightning System (Suszcynsky et al., 2001).
128 The advantage of using FORTE satellite observations is that its Low Earth Orbit (LEO) vantage
129 point is not subject to the regional biases of LMAs. However, Light and Jacobson (2002) only
130 had a small sample on the order of 1000 coincident lightning events available, which was not
131 sufficient to examine variations in lightning altitude across the globe.
132 In this study, we apply the same approach as Jacobson et al. (1999) and Light and
133 Jacobson (2002) to our comprehensive catalog of joint RF-optical FORTE detections to produce
134 document the lightning altitudes across the globe. This initial overview of our new global
135 lightning altitude dataset will focus on regional and seasonal variations in the source altitude
136 distribution, and the altitudes of lightning flashes. Future work will explore other applications of
137 the FORTE lightning altitude data.
138

139 **2 Data and Methodology**

140 2.1 The FORTE Satellite

141 The FORTE satellite was launched into a nearly circular orbit with a 70º inclination and
142 825 km altitude in August 1997. It recorded both optical and VHF lightning events from 1997
143 until 2003, and optical-only events until 2010. FORTE was unique not only for providing both

optical and RF lightning measurements of lightning from the same apace-based platform, but also for being operated in a variety of modes while on-orbit. The FORTE instruments could be commanded to operate autonomously or have one instrument trigger another, the record lengths and threshold settings could be changed while on-orbit, or individual instruments could be turned off to conserve on-board memory for the remaining sensors. As a result, the FORTE dataset is heterogeneous, and only a small fraction of the lightning events observed by FORTE have coincident detections from the FORTE RF system as well as both sensors that comprise the FORTE Optical Lightning System (OLS). These instruments and their operating modes are described below.

2.1.1 The FORTE Lightning Location System

The first OLS instrument that we will discuss is the FORTE Lightning Location System (LLS) (Suszcynsky et al., 2000). The LLS was a pixelated lightning imager whose role was to geolocate lightning events to within a nominal pixel (~ 10 km) over its 80° FOV. It was built from modified hardware from NASA's Lightning Imaging Sensor (LIS: Christian et al., 2000), with a front-end optical assembly and Charge Coupled Device (CCD) imaging array identical to LIS and an operations and signal processing module designed by Sandia National Laboratories.

Like LIS, the LLS operated autonomously and triggered whenever the signal amplitude in one of the pixels on its 128x128 imaging array during one of its 2.47 ms integrating frames exceeded a threshold above the background value. However, unlike LIS, flash clustering and background characterization was not performed, and thus could not inform the LLS signal processing. As a result, the LLS could not take advantage of cluster-based energetic particle and glint filters like the LIS filters described in Christian et al. (2000). The SNL signal processing

166 module did not screen for energetic particles, and the FORTE operators, instead, elected to turn
167 the LLS off during certain orbits that took FORTE through the South Atlantic Anomaly.
168 Moreover, a very simple and severely-limiting glint filter was implemented where individual
169 LLS pixels would be turned off once they were illuminated for three-or-more consecutive
170 frames. As a result, long-lasting lightning processes like Continuing Current (Bitzer, 2017) were
171 not as well captured by the LLS as they were with LIS.

172 Since flash clustering was not performed during the FORTE mission, we constructed
173 cluster feature data for the LLS in Peterson et al. (2021a,b). We first converted the LLS
174 detections that were termed "events" in the LLS literature (Suszcynsky et al., 2000), but were
175 more akin to LIS series features (Peterson and Rudlosky, 2019), into the single-pixel, single-
176 frame features that are termed events in the LIS literature (Christian et al., 2000; Mach et al.,
177 2007). Next, we clustered these extracted events into "groups" describing contiguous regions of
178 cloud illumination in a single integration frame, "series" that describe periods of sustained
179 illumination over time, flashes that approximate distinct lightning flashes, and "areas" that
180 approximate individual thunderstorms.

181 2.1.2 The FORTE Photodiode Detector

182 The second instrument in the OLS payload was the FORTE photodiode detector (PDD).
183 The PDD measured broadband (0.4 μm – 1.1 μm) optical waveforms from lightning events over
184 its 80° circular Field of View (FOV), which covered a ~1200 km footprint on the surface of the
185 Earth (Kirkland et al., 2001; Suszcynsky et al., 2000). The PDD had a sampling interval of 15

186 microseconds and a variable record length. Under autonomous triggering, PDD records captured
187 1.92 ms of data, while external triggers produces 6.75 ms records.

188 The PDD rejected false events from energetic particle impacts by requiring that the PDD
189 signal exceed the background threshold over a specified number of samples ranging from 0 (off)
190 to 32. However, a typical value during the FORTE mission was 5, equating to 75 microseconds.
191 The PDD was also subject to trigger rate limitations including a minimum dead time
192 approximately equal to the record length between successive triggers, and a configurable limit on
193 the maximum number of triggers allowed over a short time interval. Once this latter limit was
194 reached, the PDD would stop triggering until it received the next GPS-derived 1-Hz signal
195 (Kirkland et al., 2001). While nominally employed to mitigate glint artifacts, this limit also
196 prevented the FORTE PDD from capturing later activity in lightning flashes.

197 As with the LLS, we constructed cluster feature data for the PDD in Peterson et al.
198 (2021a,b). However, the exceptional temporal sampling of the PDD allowed us to expand the
199 data tree to finer scales by defining smaller-scale features than the typically ~2 ms events. The
200 basic unit of PDD clustering becomes the 15-microsecond "sample" feature, which cluster into
201 "pulses" that will be described in Section 2.2.

202 2..1.3 The FORTE RF System

203 The FORTE RF system consisted of two different types of broadband VHF receivers: the
204 Two And Twenty Receiver" (TATR) and the "HUndred Megahertz Receiver" (HUMR). These
205 receivers were connected to FORTE's two identical Log-Periodic Antennas (LPAs) that were
206 mounted orthogonal to each other along the nadir-pointing boom (Jacobson et al., 1999;
207 Suszcynsky et al., 2000; Shao and Jacobson, 2001; Light et al., 2001b). TATR and HUMR

208 recorded VHF waveforms from global lightning from late 1997 until 2003 across a 20 – 300
209 MHz band.

210 The TATR payload consisted of two receivers (TATR-A and TATR-B) that would each
211 sample one of the FORTE LPA antennas. Each receiver could be independently tuned, and
212 would provide VHF measurements across a 22-MHz subband. In addition to tuning, TATR
213 record lengths and the ratios of pre-trigger to post-trigger samples were also reconfigured
214 throughout the FORTE mission, providing a heterogenous collection of VHF measurements from
215 global lightning events. The HUMR payload consisted of a single receiver that sampled a wider
216 85 MHz band. As with TATR, HUMR could be tuned to different frequencies across the VHF
217 spectrum. However, HUMR records were also generally longer than TATR records. The longer
218 6.75 ms PDD records mentioned previously were coincident with HUMR records of a
219 comparable length.

220 The FORTE RF system had multiple triggering modes including a manual trigger mode
221 for on-orbit testing, an external trigger mode to capture RF waveforms from OLS events, and an
222 autonomous trigger mode. These different modes are summarized in Light (2020). The
223 autonomous trigger mode leveraged the wideband nature of lightning pulses to screen for
224 terrestrial noise, which tends to be comprised of narrowband carrier signals. The wideband RF
225 signal was divided into eight evenly-space 1-MHz channels across the receiver passband. RF
226 power was monitored in each of these channels, and an “alarm” was issued whenever the power

in one of the channels exceeded a noise-riding threshold. If multiple channels (usually 5) produced simultaneous alarms, the RF system would trigger and report an event.

RF events and their waveform records are also clustered into features like the PDD and LLS data. The RF "sample" and "pulse" features will be described in the next section. Finally, all of the cluster features from each of the three FORTE instruments are cross-linked to facilitate comparisons between sensors.

2.2 Signal Processing and Pulse Extraction

Both the PDD and RF system provide waveform data for each recorded event that might contain one or more distinct pulses from various lightning phenomena. In the original clustering described in Peterson et al. (2021a), we identified pulses as features bounding contiguous samples that exceeded the background value by a specified threshold. This approach was applied directly to the PDD irradiance data, and to the RF data after signal processing. The RF waveforms were first "prewhitened" to remove manmade carrier waves from the wideband measurements and then "dechirped" to counteract the frequency-dependent delay in the signal time of arrival from propagation through the ionosphere. These standard procedures in FORTE studies are described in Light (2020). Pulses were then identified in the timeseries of average power across the band. For the TATR data, where we have 2 independent waveforms from each event, we use only the waveform that has the greatest signal amplitude to extract pules.

While this approach is sufficient for simple PDD and RF waveforms dominated by discrete high-amplitude pulses, it is not well-suited for distinguishing pulses in complex waveforms that contain multiple pulses of varying amplitude, spacing, and effective width. Therefore, we developed new approach that could be applied to either the PDD or RF data to

extract and characterize pulses over a variety of waveform shapes. Pulses and their child "peak" features are found by looping from the maximum signal amplitude down to the noise threshold. A new pulse feature is created when samples are found that both exceed the incremental threshold and do not occur within a specified time threshold of an existing pulse. If a new pulse is not identified, the existing pulses are expanded to include the new samples that exceed the incremental threshold. This new approach permits a single contiguous portion of the waveform that contains multiple prominent peaks separated in time to be partitioned into two or more pulse features. The old approach would always identify a single pulse feature in these complex waveforms.

To demonstrate pulse extraction, Figure 1 shows an example dechirped TATR waveform that contained two Trans-Ionospheric Pulse Pairs (TIPPs) from in-cloud lightning events and a third solitary pulse. The band-averaged power timeseries (solid black line) is first smoothed (solid red line), and the pulse feature threshold is determined as 3x the standard deviation above the minimum value in the smoothed curve (top dashed horizontal line). The iterative threshold method described above identifies 5 peak features (solid blue lines) in 5 pulse features (blue bars in Figure 1b with dashed vertical lines indicating their endpoints). Pulse characteristics are then computed using windows that encapsulate the pulse plus a 20 microsecond buffer on either side (grey boxes in Figure 1b). Finally, TIPPs are identified as impulsive features that are in close temporal proximity to another impulsive feature. The constituent pulses in each TIPP are then linked (solid horizontal black lines in Figure 1b), and the peak-to-peak time difference for the TIPP is recorded.

In TIPP cases where multiple candidate links might be made (as with pulses 3 and 4 in Figure 1b), feature links are prioritized by minimizing a Weighted Euclidean Distance (WED)

function of the differences in time and feature attributes (i.e., pulse width, peak power, rise time, etc.). In Figure 1b, Pulse 3 was linked to Pulse 4 because it produced the lowest WED values of the remaining features, even though Pulse 4 was a better match for Pulse 5. A common cause of these differing links is that only one of the pulses in the TIPP exceeded the noise threshold, which appears to be the case here. To mitigate this potential source of uncertainty in the pulse separation times, we only consider TIPPs where both constituent pulses identify the other as its partner, as with Pulse 4 and Pulse 5. The two pulses that comprise each linked TIPP are integrated into a single entry in our feature database.

Applying these methods to all types of RF events in the FORTE record produces the pulse statistics shown in Figure 2. Events whose power timeseries were too flat to produce any pulse features are not considered. Most of the remaining events contain only 1 or 2 pulses (Figure 2a) – with a peak at 2 due to the prevalence of TIPPs in the data. However, the remaining 40-50% events (depending on the category) contain more than 2 pulses. These may be trains of weak TIPPs from in-cloud events, a Cloud-to-Ground (CG) stoke with a TIPP, or a diffuse in-cloud event (i.e., a K-change) with embedded impulsive in-cloud events. The longer events in the FORTE RF record that last multiple milliseconds can contain dozens of distinct pulses. The number of individual peaks in a given pulse (Figure 1b) also varies by pulse type. Nominally, each pulse will have a single peak per pulse (or 2 peaks per TIPP). However, 17% of pulses have 3-or-more peaks. Analyzing these events (not shown for brevity) indicates that they tend to be mixed events where the peaks (including TIPPs) were not sufficiently isolated in time from the other nearby peaks to create separate pulse features.

Pulse features also have a wide range of effective widths (Figure 2c). The median effective width for an individual pulse in a TIPP is 8 microseconds, and the prevalence of TIPPs

295 in the FORTE data heavily biases the general pulse width statistics. Only ~40% of general pulses
296 in our database have effective widths exceeding 40 microseconds, with the peak at 40
297 microseconds being artificial due to the thresholds used in the algorithm. These thresholds also
298 control the minimum signal amplitude that results in a pulse being identified (Figure 2d). Few
299 general pulses and hardly any TIPPs are resolved with a peak amplitude < 2 dB above the noise
300 threshold. Most pulses exceed the threshold by at least 5 dB. Pulses like Pulse 1 and 2 in Figure
301 1b are more common in our dataset than Pulses 4 and 5 because the threshold is set fairly high
302 compared to the actual noise floor in order to reduce the number of spurious events. This also
303 means that, while we do not restrict our sample to lowband (20-50 MHz) TATR detections, these
304 events dominate because lightning is more powerful in the lowband and the HUMR waveforms
305 tend to be noisier than TATR waveforms.

306 These pulses also occurred throughout the RF event record (Figure 2e). The most
307 common location in the record was around 25% of the record length, with increased frequencies
308 earlier in the record compared to later. This is due to both the commanded pretrigger fraction and
309 the dechirping process pushing the signal back to its vacuum time of arrival. Higher TEC values
310 will result in larger temporal displacements than lower TECs. This can pose a problem for
311 characterizing pulses at the beginning of the RF record. The initial portion of a broader pulse or
312 the first constituent pulse of an early TIPP can be rolled around to the end of the record by the
313 dechirping algorithm. This is why there is a second peak in Figure 2e at the end of the record. It
314 is not physical, but rather an artifact of dechirping.

315 Pulses traversing the ionosphere along paths with high TEC values were observed by
316 FORTE due to its global observation domain and large effective FOV (Figure 2f). Our identified
317 pulses were subject to TEC values ranging from near 0 TECU to greater than 120 TECU (Figure

2f). Moreover, the dechirp algorithm failed in certain events, while there were other events that resulted from onboard discharges on the spacecraft . Both of these scenarios yield a reported TEC ≤ 0 TECU, and are shown in the rightmost bin in Figure 2f.

2.3 Filtering LLS-Coincident RF Events

The pulse statistics in Figure 2 indicate that we can use automated routines to create a robust sample of distinct RF pulses from the FORTE data. However, these pulses need to be filtered to ensure that the VHF source altitudes are physically meaningful. Pulses that lack LLS coincidence will not be useful. Meanwhile, pulses that occur at the beginnings or ends of the record, or that report a TEC ≤ 0 TECU will yield questionable pulse time differences.

However, the FORTE sampling of global pulses is already uneven – due in large part to the heterogeneous FORTE commanding – and filtering the RF data further impacts the global distribution of detected VHF sources. Table 1 summarizes the pulse counts in our global sample. In total, 3 million distinct pulses are identified including 1 million TIPPs (36% of all pulses). Figure 4 shows global distributions of RF events with pulse features (Figure 4a), all RF pulse features (Figure 4b), and RF TIPPs (Figure 4c) according to the FORTE satellite subpoint. While FORTE detections of the pulses in Table 1 are generally concentrated in the tropics, and particularly around the tropical landmasses of the Americas, Africa, and the Maritime Continent, all three global source distributions differ substantially from lightning climatologies derived from NASA sensors (Cecil et al., 2014; Albrecht et al., 2016; Peterson et al., 2021c). Perhaps the most notable departures occur in Africa, where VHF sources are prevalent in west Africa while being infrequent in the primary lightning hotspot of the Congo Basin. Additionally, horizontal

striping can be noted in the Indian Ocean and Asia where RF detections are concentrated within a latitude band surrounding the equator. A second band is also apparent in the Southern Ocean.

LLS coincidence is required to compute source altitude, but this requirement convolutes the sampling biases from the two sensors. To minimize these biases to the extent possible while preserving a reasonable sample size, we elect to take a "flash-level" approach to defining LLS coincidence. We treat the RF event as an "event" feature in the LLS clustering scheme, which is based on LIS clustering in Christian et al. (2001). All LLS events that occur within 330 ms of the RF pulse are assumed to be candidates for the location of its origin. We compute this location as the radiance-weighted mean position of all events that occur in the prescribed time window. Under normal circumstances, all of these events would come from the same parent flash, or at least the same parent thunderstorm area, and the RF source would be geolocated to a point within 10-30 kilometers of its true location. However, it is possible to have multiple ongoing thunderstorms producing events within the LLS FOV at the same time. When this occurs, the RF source location is weighted towards the more active thunderstorm.

Of the original 1 million RF TIPPs, the flash-level LLS coincidence requirement limits the sample size to 380,000. These are the "TIPPs with LLS" entries in Figure 2. These LLS-coincident TIPPs have similar effective width statistics to normal TIPPs (Figure 2c), are somewhat more powerful (Figure 2d), and their times similarly peak at 25% of the record length (Figure 2e), indicating that they were commonly the triggering pulse. However, their slant TECs in Figure 2f are significantly lower than the 20-30 TECU medians for the other pulse categories. This is due to two known biases imposed by the LLS: (1) the smaller 80° LLS FOV removed events that originate near the limb and traverse nearly horizontally through the ionosphere (experiencing high TECs) from the sample and (2) the LLS being more capable of detecting

lightning at night (when TECs are low) compared to during the day (when TECs are high). Diurnal performance differences were also an issue with LIS that had to be compensated for when creating the global lightning flash rate climatologies (Cecil et al., 2014; Albrecht et al., 2016; Peterson et al., 2021c).

If we exclude pulses that have invalid TECs or that occur in the first or last 5% of the record, we are left with 2.4 million events, 907,083 of which (37%) are TIPPs. Of these TIPPs, 300,214 have LLS coincidence at the flash level. Finally, if we further exclude pulses that occur within 100 microseconds of another pulse (like Pulse 3 in Figure 1), the sample size is reduced to 1.8 million pulses and nearly 695,146 TIPPs (39%), 202,062 of which have LLS coincidence. We can also optionally require that only a single LLS flash or LLS area is active at the time of the RF event. This further reduces the sample to 152,995 LLS-coincident TIPPs at the area level and 130,261 LLS-coincident TIPPs at the flash level. This filtering leaves us with 100k - 200k TIPPs from across the globe that we can use to compute the VHF source altitudes, a sample that is two orders of magnitude larger than Light and Jacobson (2002).

2.4 Calculating the Altitudes of Global VHF Sources

Jacobson et al. (1999) derived the following equation for the altitude of the VHF source responsible for a TIPP:

$$a = c \cdot \tau \frac{\sin \beta}{1 - \cos 2\beta}$$

where c is the speed of light, τ is the time delay between the pulses that comprise the TIPP, and β is the satellite elevation angle, which can be computed from the satellite position and the

latitude and longitude of the source. This equation assumes a spherical Earth where the source is close to the surface.

Our use of flash-level LLS coincidence to geolocate the source is only justified as long as the locations errors geolocating to the wrong part of the storm or flash (i.e., a few tens of kilometers) only result in small altitude errors. To test this, we compute the altitude of a TIPP with a 20 microsecond pulse separation at each point across the LLS FOV in Figure 4a, and then the altitude error that would result from the TIPP being offset 10 km radially outward from its true position in Figure 4b. Within the limited 80° LLS FOV, the maximum error in altitude for being displaced by 10 km is only expected to be around 60 m. Therefore, we can be off by even a few tens of kilometers without observing a notable effect on the altitude statistics.

The key parameter to measure precisely is the time difference between the two peaks in the TIPP. Figure 4c computes the altitude error from being off by just 1 microsecond for a source at each point on the LLS imaging array. Each microsecond of error results in an altitude error of between 150 m at nadir to 350 m at the edge of the LLS FOV. It only takes a 3 microsecond error for an edge source to be displaced in altitude by a full kilometer.

3 Results

The following sections will document the FORTE distributions of lightning altitudes derived from LLS-coincident VHF source data. Section 3.1 will examine global distributions of VHF source altitude. Section 3.2 will consider variations in the lightning altitude distributions

between different regions of the Earth and between each season. Section 3.3 will examine the VHF source altitude distributions from LLS flashes.

3.1 Global Distributions of VHF Lightning Source Altitude

The FORTE orbit covered all of the major lightning-producing regions of the Earth, but these regions were not sampled consistently, as we saw in the global distributions of RF events and pulses in Figure 3. Requiring LLS coincidence substantially reduces the sample of events, which can be noted in Table 1. The global distribution of LLS-coincident RF TIPPs is shown in Figure 5. Figure 5a is analogous to the plots from Figure 3, except the FORTE satellite subpoint position is replaced with the geolocated LLS position. The same RF event hotspots in the Americas, west Africa, and the Maritime Continent can be noted, but the LLS coincidence requirement removes the horizontal banding in the distribution while limiting the number of samples at mid to high latitudes (particularly over the Eurasian continent).

Source altitude distributions by latitude (Figure 5b) and longitude (Figure 5c) are shown to the right of and below the global distribution in Figure 5a, while the global altitude profile is plotted in Figure 5d. Source altitudes are dominated by the upper charge layer at 10-12 km altitude, which is normally positively charged and where negative leaders that are good emitters of VHF radiation propagate. Light and Jacobson (2002) also identified peaks in their VHF emitter altitude profiles in this range. Lower-altitude sources are less frequent and are usually found between 5 km and 10 km.

However, not all regions conform to the global profile in Figure 5c, and some regional differences can even be noted in the overall latitude (Figure 5b) and longitude (Figure 5c) distributions. Low-altitude sources are more common over the longitude range associated with

424 the Americas chimney region compared to the Maritime Continent chimney region. While the
425 Africa chimney in the Congo Basin is not well resolved, the west Africa maximum has a greater
426 proportion of low-altitude sources along the west African coast compared to in the east over the
427 continent. The source distributions also tend to be taller at low latitudes near the equator in
428 Figure 5b compared to the mid-latitudes where, a subtle low-altitude peak at 6 km altitude is
429 faintly visible.

430 3.2 Regional and Seasonal Variations in Lightning Altitude

431 Due to the uneven sampling of the data, we will focus our discussion around altitude
432 profiles that have first been normalized by the local event count (i.e., Figure 5d). Twelve global
433 regions are boxed in Figure 5a that roughly correspond to the northern hemisphere mid-latitudes,
434 the northern hemisphere tropics, the southern hemisphere tropics, and the southern hemisphere
435 mid-latitudes for the three continental chimneys: the Americas, Europe and Africa, and Asia. The
436 VHF source altitude profiles for each of these regions are shown in Figure 6 organized
437 horizontally by longitude and vertically by latitude.

438 The source altitude distributions in these regions differ from the global altitude profile in
439 Figure 5d. The continental United States (Figure 6a) has a pronounced plateau between 5 km and
440 10 km similar to the NLDN-matched profile in Light and Jacobson (2002). The other mid-
441 latitude regions such as South Africa (Figure 6k) and southern Australia (Figure 6l) also have
442 enhanced activity at low altitudes, and low-level activity even dominates in mid-latitude regions
443 where a large fraction of the sources come from over the ocean - including the North Atlantic /
444 Mediterranean Sea (Figure 6b) and the northern Pacific Ocean (Figure 6c). The La Plata basin is
445 unique because its thunderstorms form over land where they may grow upscale into large

Mesoscale Convective Systems (MCSs) before moving offshore. Its altitude profile is heavily weighted towards low-altitude sources, with a peak at 7 km. However, this is not due to the contribution of oceanic thunderstorms. When the oceanic sources are removed, the peak only increases to 8 km altitude.

There are a few potential explanations for the La Plata basin having such a low source altitude profile. The most problematic would be contamination from South Atlantic Anomaly (SAA) artifacts causing errors in the LLS source location. SAA artifacts manifest as single-pixel detections or detections along a streak of pixels that are random and isolated in time to an instrument like the LLS. Due to this randomness, they are not expected to consistently displace the source location towards the center of the array where the altitude corresponding to a given intra-pulse time difference would be lower (i.e., Figure 4a). Moreover, we can remove this potential source of error by only plotting the intra-pulse time for each TIPP. When we replace source altitude in Figure 6 with intra-pulse time, the La Plata basin altitude profile also has smaller time delays between pulses, leading to a comparable shape to the altitude profile in Figure 6j. The larger share of low-altitude VHF sources in the La Plata basin appears to be legitimate.

We suggest that this increased fraction of low-altitude sources is due to the prevalence of stratiform lightning. In addition to the upper positive charge layer, negative leaders also propagate through regions of positive stratiform charge. However, while this propagation is confined to a small area in convective cases, stratiform leaders can propagate over hundreds of kilometers (Lang et al., 2017; Peterson, 2019; Lyons et al., 2020). Our previous analysis of an oceanic megaflash in the FORTE record showed that the flash constantly emitted VHF radiation in multiple periods of sequential triggering (i.e., series) that each lasted tens to hundreds of

469 milliseconds. The impulsive VHF sources that we could identify were clustered in a layer around
470 4-8 km altitude (Peterson et al., 2021a), consistent with Figure 6j. While megaflashes occur in
471 many regions, the La Plata basin is one of the primary Americas hotspots (Peterson, 2021;
472 Peterson and Stano, 2021) – along with the Continental United States, which also has an
473 increased share of low-altitude sources in Figure 6a. We have also recorded long horizontal
474 lightning over the Mediterranean Sea (Peterson et al., 2017a) (Figure 6b) and showed that the
475 remaining mid-latitude oceanic regions with increased low-altitude source fractions in Figure 6
476 are also locations with long horizontal flashes (Figure 5 in Peterson et al., 2017b).

477 The tropical regions in Figure 6, by contrast, are more heavily weighted towards higher
478 altitudes corresponding to the upper positive charge layer. However, the source altitude profiles
479 still different between these tropical regions. If we rank these regions by the 75th percentile VHF
480 source altitude, Panama / Colombia (Figure 6d) has the overall tallest thunderstorm charge
481 structures (13.6 km), followed by the Maritime Continent (Figure 6i; 13.0 km), the Continental
482 United States (12.6 km), and then the Congo Basin (Figure 6h; 12.6 km) and West Africa (Figure
483 6e; 12.5 km). The Amazon Basin (Figure 6g) has a nearly identical 75th percentile source altitude
484 as the joint India / the Indian Ocean region (Figure 6f) of 12.4 km in either case. The Amazon
485 has a larger share of low-altitude sources and, despite this higher 75th percentile altitude, the
486 mode is only at 10 km altitude.

487 Figure 7 maps these 75th percentile source altitudes (Figure 7a) for each gridpoint in
488 Figure 5 along with the median (Figure 7b) and 25th percentile (Figure 7c) values. Pixels with
489 less than 10 sources are not shown. The large regional domains used in Figure 6 obscure the fine-
490 scale structure caused by thunderstorm interactions with the local terrain. There is a marked
491 difference between the land-based and oceanic source altitude profiles. Tropical oceanic

thunderstorms can be just as tall as land-based storms over the Caribbean Sea, Gulf of Mexico, Indian Ocean, and Pacific Ocean. At the same time, oceanic storms at higher latitudes (and in the Atlantic Ocean between the Americas and Africa) tend to be quite shallow.

Much of the mid-latitude behavior is due to seasonal trends. Figure 8 shows latitude-altitude profiles for land-based, the coastal ocean (within 1000 km of the continents) and the open ocean (beyond 1000 km) averaged over 3-month periods. The profiles for each latitude are normalized according to the total number of detected sources such that all columns in each panel sum to 100%. The land-based source altitude profiles (left column) extend up to high altitudes during the summer season with a dominant upper positive charge layer above 10 km. During the winter, source altitudes are concentrated at lower altitudes around 5 km. The passage of the seasons causes the summer upper and winter lower maxima to move in latitude, following the increased insolation. The apparent slant in the distribution during northern hemisphere fall, winter, and spring is due to the prevalence of low-altitude sources in the southern hemisphere (i.e,. La Plata, South Africa, and Southern Australia) regions discussed previously. The coastal ocean profiles, meanwhile, are similar to their land-based counterparts, and we can also see similar seasonal behavior with the open ocean profiles (right column), though data is sparse from these low flash rate thunderstorms far from shore.

3.3 Initiation and Propagation Altitudes in LLS Flashes

We previously demonstrated that FORTE is capable of documenting the evolution of individual flashes (Peterson et al., 2021a,b). We used LLS to resolve the lateral development of the leaders in the flash (as with LIS in Peterson et al., 2018) and then applied the altitude algorithm to intracloud events that were identified and had their intra-pulse delays measured by

514 hand. In this section, we will follow the same procedure using pulses that were automatically
515 identified, linked, and assigned to LLS flashes.

516 An example of a particularly well-resolved flash is shown in Figure 9. Source altitudes
517 before (Figure 9a), during (Figure 9b), and after (Figure 9c) are shown for the flash of interest
518 (blue) and other flashes (red). We normal only consider isolated sources that do not have pulses
519 within 100 microseconds of the TIPP. However, to provide a more complete picture of VHF
520 activity in the flash, we show these potentially ambiguous sources in black in Figure 9b. The
521 extent of the LLS flash at each point in time is also overlaid as a line plot. VHF sources are
522 mapped in Figure 9d and colored according to whether they occurred in the flash of interest and
523 whether they occurred above or below 9 km altitude. Finally, a source altitude distribution is
524 shown in Figure 9e.

525 This flash case occurred in a thunderstorm over the Pacific Ocean on 7/12/2001. It started
526 with an RF-powerful TIPP at 7 km altitude followed promptly by activity in the upper positive
527 layer that was resolved by the LLS (line in Figure 9b). If we assume that these initial sources
528 bound the breakdown of the negative leader, then the approximate vertical speed of the
529 developing leader was 6.2×10^5 ms^{-1}, which is consistent with the previously-reported vertical
530 speeds for negative leaders. Infrequent activity can also be noted in in a lower (apparently
531 negative) layer around 6 km altitude, and between the two layers. Since the first source from the
532 lower layer was ambiguous (black in Figure 9b), our filtered dataset would identify the first
533 activity in this lower activity as occurring 300 ms into the flash. Due to the low frequency of
534 sources from the lower negative layer, reductions in source counts from ambiguous negative
535 events have a greater impact on our statistics than positive sources. There were no other flashes
536 before the flash of interest, but a few were detected in the 30 s after it ended. These flashes had

similar altitude profiles (Figure 9e) to the flash of interest, with a high concentration of sources around 12 km altitude and comparably few low-altitude sources.

Analyzing FORTE flashes like the cases in Figure 9 and Peterson et al. (2021a,b) demonstrate that space-based platforms like FORTE are capable of resolving the flash phenomena that are required for automatically resolving thunderstorm charge structure with algorithms like chargepol. This was even demonstrated in Figure 21 Jacobson et al. (1999), though a lack of geolocation information meant that the flash evolution was mapped in units of intra-TIPP time rather than altitude. However, even the particularly well-resolved flash in Figure 9 also demonstrates the difficulties in applying these methods to on-orbit data. The first issue is view time. Chargepol accumulates LMA data over time to derive the bulk electrical structure of the thunderstorm. However, space-based platforms are only in view of a given thunderstorm for a few minutes, and there might not be enough data during the overpass to generate robust statistics – particularly from low flash rate oceanic storms. Another issue is that the level of detail provided by a space-based platform is considerably less than what would be seen by a typical LMA due to the increased range. Even in this case where we have dozens of sources (which is rare), only 3 sources occur in the initial breakdown period (one of which is ambiguous). There is not enough data to confidently resolve the upward propagation of the negative leader in most FORTE flashes.

While we lack sufficient sources to characterize the initial breakdown of the negative leader for individual flashes, we can still examine its statistical behavior by aggregating the source altitude distributions from multiple flashes. Figure 10 computes the VHF cumulative altitude distributions for each point in the durations of flashes over land (top row), over the coastal ocean (middle row), and over the open ocean (bottom row). The left column uses linear

560 temporal bins to detail the initial 60 ms of the flash, while the right column accumulates data in
561 logarithmic bins out to 1 s after the flash start. Note that while these VHF sources are tied to
562 individual LLS flashes, the time of flash start is the time of the first RF source linked to the flash,
563 not the start of the optical emissions detected by the LLS. Median values are also indicated with
564 solid white lines.

565 The initial breakdown phase is evident as an increase in the overall source altitude
566 profiles over the first ~20 ms of the flash. This can be seen in flashes over land (Figure 10a), the
567 coastal ocean (Figure 10c) and the open ocean (Figure 10e), but with different slopes that should
568 correspond to the speed of the negative leader. If we fit the median altitude in the first 15 ms of
569 the flash to a linear model (black line), we get typical leader propagation speeds of 1.07×10^5 ms^{-1}
570 over land, 1.31×10^5 ms^{-1} over the coastal ocean, and 1.90×10^5 ms^{-1} over the open ocean. These
571 are all within the range reported by Shao and Krehbiel (1996). The apparent difference in
572 propagation speed between land and ocean regions is apparently linked to differences in flash
573 initiation altitude. Previous studies have noted cases of particularly fast negative leaders in
574 oceanic return strokes (for example, Wu et al., 2021). However, additional data is needed to
575 verify whether this trend is physical. After the initial breakdown period, the distributions become
576 flat, with little change in the source altitude profile over time (right column). While we see cases
577 of negative leaders sloping downward later in certain flashes (including the case in Figure 9), this
578 behavior does not occur in all flashes, and it occurs at random times where it is observed –
579 causing the lack of appreciable trend in the statistics.

580 The times in Figure 9 are based on the RF events that occurred during an LLS flash.
581 Figure 10, instead, computes the altitude profiles at each point relative to the first (left column)
582 and last (right column) LLS groups in the flash. We have shown previously that the most intense

583 optical emissions frequently occur in these first or last groups (Peterson and Rudlosky, 2019).
584 This is probably due to limitations on the types and altitudes of pulses that the pixelated lighting
585 imager can detect. LIS, for example, is known to trigger late in the flash while it is developing at
586 high altitudes (Thomas et al., 2000). There is no physical reason why the first LIS or LLS group
587 should rank as one of the most energetic pulses in the flash. However, if all of the early activity
588 in the flash leading up to the first pulse with comparable energy to a stroke is too faint to detect,
589 then bright events would cluster in the first group. We see in Figure 10a,c,d that the median RF
590 source altitudes before first light are around 10 km and there is no clear trend in the source
591 altitude distribution over time. This is consistent with the idea that the size and intensity of the
592 optical emitter, rather than its altitude, are the primary factors that contribute to this first
593 detection.

594 By contrast, the source altitudes relative to the end of the flash slope downwards over
595 time. The median source altitude associated with the final LLS group is close to 10 km in land
596 (Figure 11b) and coastal ocean (Figure 11d) regions – consistent with the approximate altitude
597 where optical coincidence was previously reported to fall off (Light and Jacobson, 2002). The
598 median source altitude at the time of the final LLS group in flashes over the open ocean is lower
599 at ~8 km, but the trend is otherwise similar to the land and coastal curves. We previously noted a
600 change in the behavior of LLS groups after the upper charge layer became apparently cut off
601 following the first return stroke in a hybrid CG flash (Peterson et al., 2021b). Before the stroke,
602 frequent dim emissions were detected as the flash developed through the upper charge layer.
603 This changed to only a few large and bright groups after the stroke when only the lower charge
604 layer was active. The statistics in Figure 11b,d,f suggest that the cessation of high-altitude
605 sources late in the flash is common in the FORTE record. Therefore, a likely explanation for the

606 final group in an LLS / LIS flash being particularly bright that it corresponds to the stroke or
607 other energetic process immediately before the high-altitude portions of the flash become cut off,
608 and any subsequent activity from the lower layer is too dim for the imager to detect.

609 Finally, we compute the initiation and propagation altitudes for these FORTE flashes. To
610 allow for errors from spurious sources, we define the initiation altitude as the lowest altitude of
611 all sources during the initial breakdown phase within 15 ms of the flash start. Then, the
612 propagation altitude is defined as the average altitude of all sources in the LLS flash. For this
613 analysis, we will allow the ambiguous sources (black dots in 10b) to better resolve activity in the
614 negative charge layer. Profiles of initiation altitude (left column) and propagation altitude (right
615 column) are shown in Figure 12 for flashes over land (top row), the coastal ocean (middle row)
616 and the open ocean (bottom row).

617 The initiation altitude profile for land-based flashes has two peaks: a lower peak at 7 km
618 altitude, and an upper peak at 10-11 km altitude. Oceanic flashes are more likely to have their
619 initial sources at low altitudes, as we saw in Figure 12. The lower peak (6 km altitude) is
620 dominant over the upper peak for the coastal ocean (Figure 12c), while the upper peak is hardly
621 apparent for flashes over the open ocean (Figure 12e) where the lower peak is further reduced to
622 4 km altitude. The peaks in the propagation altitude distribution, meanwhile, are similar between
623 land and the coastal ocean, though the oceanic flashes are still more likely to propagate at lower
624 altitudes, overall. The propagation altitude profile for flashes over the open ocean is single-
625 peaked with a maximum at 7 km altitude.

626 These altitude profiles do not consider variations in flash initiation or propagation
627 altitudes by flash type (intracloud or Cloud to Ground) or storm type (as in Mecikalski and

628 Carey, 2018), which jointly vary by region of the Earth. Flash type and storm type partitioning
629 are topics that we plan to consider in future work.

630

631 **5 Conclusion**

632 We leverage coincident detections of lightning events by the FORTE RF system and LLS
633 to document the altitude distributions of in-cloud lightning sources across the globe. Previous
634 FORTE studies generated profiles of VHF source altitudes (Light and Jacobson, 2002) but were
635 limited by a small sample size. Using the full FORTE RF record and relaxing the criteria for LLS
636 coincidence, we are able to characterize the vertical distributions of VHF sources over large
637 swaths of the Earth's land and ocean regions.

638 The negative leaders that are prevalent emitters of VHF radiation most often propagate
639 through the upper positive charge layer of ordinary thunderstorms. For this reason, the FORTE
640 VHF source altitude distributions generally peak at 11 km altitude. However, VHF sources at
641 lower altitudes including initial breakdowns and later activity in the lower negative charge layer
642 can also resolved from space. We also find that typical vertical development speeds of these
643 negative leaders appear to differ between land (1.07×10^5 ms^{-1}), coastal oceanic regions (1.31×10^5
644 ms^{-1}), and the open ocean (1.90×10^5 ms^{-1}). However, while FORTE can resolve the lightning
645 phenomena required for automated charge layer identification with the chargepol algorithm
646 (Medina et al., 2021), the level of unambiguous detail we can resolve is usually not sufficient to
647 characterize the upward developing leader on a per-flash basis, and the limited viewtime
648 provided by its Low Earth Orbit (LEO) inhibits robust statistics from individual thunderstorms.

649 Low-altitude sources are found to be particularly common in winter and/or oceanic
650 regions outside of the tropics, as well as over the La Plata basin where large MCSs produce
651 abundant stratiform lightning including megaflashes. We previously showed that an individual
652 large stratiform flash can produce hundreds of FORTE RF events with their impulsive VHF
653 sources clustered in a layer between 4 and 8 km altitude (Peterson et al., 2021a). Regions with
654 frequent stratiform lightning are thus expected to have significant contributions from both high-
655 altitude convective sources and low-altitude stratiform sources. Tropical regions, meanwhile, had
656 the tallest source altitude profiles with the Colombia and Panama region having the greatest 75th
657 percentile source altitude (13.6 km) of the regions considered.

658 Regional factors including seasonal variations in storm type are shown to have a
659 pronounced impact on the VHF source altitude profiles as well as the initiation and propagation
660 heights of individual flashes. We provide a high-level overview of some of the variations in the
661 data, but further in-depth analysis is required to explain all of the trends in this new dataset. We
662 also plan to create distinct altitude profiles for CG and IC flashes as well as various storm types
663 (as in Mecikalski and Carey, 2018) in future work. It is expected that these global measurements
664 will be valuable for global climate modeling, particularly LNOx models, that currently derive
665 lightning altitudes from parameterizations based on environmental parameters. Further
666 applications of this data will also be explored in future work.

667

668 **Open Research**

669 The FORTE data used in this study are available at the Harvard Dataverse and may be accessed
670 via the DOI listed in Peterson (2022).

Acknowledgments

Los Alamos National Laboratory is operated by Triad National Security, LLC, under contract number 89233218CNA000001. The data presented in this study are located at Peterson (2022). As we celebrate the 25th anniversary of the FORTE's launch, we would like to extend a special thank you to the FORTE science team at LANL and SNL for all of their efforts over the past three decades in making the FORTE program a success.

679 **References**

680

681 Albrecht, R. I., Goodman, S. J., Buechler, D. E., Blakeslee, R. J., & Christian, H. J. (2016).
682 Where are the lightning hotspots on Earth?. *Bulletin of the American Meteorological*
683 *Society*, *97*(11), 2051-2068.
684 Bitzer, P. M. (2017). Global distribution and properties of continuing current in lightning.
685 *Journal of Geophysical Research: Atmospheres*, *122*(2), 1033-1041.
686 Carey, L. D., Koshak, W., Peterson, H., & Mecikalski, R. M. (2016). The kinematic and
687 microphysical control of lightning rate, extent, and NOX production. *Journal of*
688 *Geophysical Research: Atmospheres*, *121*(13), 7975-7989.
689 Cecil, D. J., Buechler, D. E., & Blakeslee, R. J. (2014). Gridded lightning climatology from
690 TRMM-LIS and OTD: Dataset description. *Atmospheric Research*, *135*, 404-414.
691 Chameides, W., & Walker, J. C. (1973). A photochemical theory of tropospheric ozone. *Journal*
692 *of Geophysical Research*, *78*(36), 8751-8760.
693 Christian, H. J., R. J. Blakeslee, S. J. Goodman, and D. M. Mach (Eds.), 2000: Algorithm
694 Theoretical Basis Document (ATBD) for the Lightning Imaging Sensor (LIS),
695 NASA/Marshall Space Flight Center, Alabama. (Available as
696 http://eospso.gsfc.nasa.gov/atbd/listables.html, posted 1 Feb. 2000)
697 Crutzen, P. (1973). A discussion of the chemistry of some minor constituents in the stratosphere
698 and troposphere. *Pure and Applied Geophysics*, *106*(1), 1385-1399.
699 Crutzen, P. J., Heidt, L. E., Krasnec, J. P., Pollock, W. H., & Seiler, W. (1979). Biomass burning
700 as a source of atmospheric gases CO, H2, N2O, NO, CH3Cl and COS. *Nature*,
701 *282*(5736), 253-256.

Cummins, K. L., Murphy, M. J., Bardo, E. A., Hiscox, W. L., Pyle, R. B., & Pifer, A. E. (1998). A combined TOA/MDF technology upgrade of the US National Lightning Detection Network. *Journal of Geophysical Research: Atmospheres*, *103*(D8), 9035-9044.

DeCaria, A. J., Pickering, K. E., Stenchikov, G. L., Scala, J. R., Stith, J. L., Dye, J. E., ... & Laroche, P. (2000). A cloud-scale model study of lightning-generated NO x in an individual thunderstorm during STERAO-A. *Journal of Geophysical Research: Atmospheres*, *105*(D9), 11601-11616.

Ely, B. L., Orville, R. E., Carey, L. D., & Hodapp, C. L. (2008). Evolution of the total lightning structure in a leading-line, trailing-stratiform mesoscale convective system over Houston, Texas. *Journal of Geophysical Research: Atmospheres*, *113*(D8).

Fierro, A. O., Shao, X. M., Hamlin, T., Reisner, J. M., & Harlin, J. (2011). Evolution of eyewall convective events as indicated by intracloud and cloud-to-ground lightning activity during the rapid intensification of hurricanes Rita and Katrina. *Monthly Weather Review*, *139*(5), 1492-1504.

Fishman, J., Solomon, S., & Crutzen, P. J. (1979). Observational and theoretical evidence in support of a significant in-situ photochemical source of tropospheric ozone. *Tellus*, *31*(5), 432-446.

Ivanov, M. F., Kiverin, A. D., Klumov, B. A., & Fortov, V. E. (2014). From combustion and detonation to nitrogen oxides. *Physics-Uspekhi*, *57*(3), 234.

Jacobson, A. R., Knox, S. O., Franz, R., & Enemark, D. C. (1999). FORTE observations of lightning radio-frequency signatures: Capabilities and basic results. *Radio Science*, *34*(2), 337-354.

724 Jaeglé, L., Jacob, D. J., Wang, Y., Weinheimer, A. J., Ridley, B. A., Campos, T. L., ... & Hagen,
725 D. E. (1998). Sources and chemistry of NOx in the upper troposphere over the United
726 States. *Geophysical Research Letters*, *25*(10), 1705-1708.
727 Jayaratne, E. R., Saunders, C. P. R., & Hallett, J. (1983). Laboratory studies of the charging of
728 soft-hail during ice crystal interactions. *Quarterly Journal of the Royal Meteorological*
729 *Society*, *109*(461), 609-630.
730 Kirkland, M. W., Suszcynsky, D. M., Guillen, J. L. L., & Green, J. L. (2001). Optical
731 observations of terrestrial lightning by the FORTE satellite photodiode detector. *Journal*
732 *of Geophysical Research: Atmospheres*, *106*(D24), 33499-33509.
733 Labrador, L. J., Von Kuhlmann, R., & Lawrence, M. G. (2005). The effects of lightning-
734 produced NO x and its vertical distribution on atmospheric chemistry: sensitivity
735 simulations with MATCH-MPIC. *Atmospheric Chemistry and Physics*, *5*(7), 1815-1834.
736 Lacis, A. A., Wuebbles, D. J., & Logan, J. A. (1990). Radiative forcing of climate by changes in
737 the vertical distribution of ozone. *Journal of Geophysical Research: Atmospheres*,
738 *95*(D7), 9971-99
739 Lang, T. J., & Rutledge, S. A. (2008). Kinematic, microphysical, and electrical aspects of an
740 asymmetric bow-echo mesoscale convective system observed during STEPS 2000.
741 *Journal of Geophysical Research: Atmospheres*, *113*(D8).
742 Lang, T. J., Pédeboy, S., Rison, W., Cerveny, R. S., Montanyà, J., Chauzy, S., ... & Krahenbuhl,
743 D. S. (2017). WMO world record lightning extremes: Longest reported flash distance and
744 longest reported flash duration. *Bulletin of the American Meteorological Society*, *98*(6),
745 1153-1168.

Light, T. E. L., & Jacobson, A. R. (2002). Characteristics of impulsive VHF lightning signals observed by the FORTE satellite. *Journal of Geophysical Research: Atmospheres*, *107*(D24), ACL-8.

Luo, C., Wang, Y., & Koshak, W. J. (2017). Development of a self-consistent lightning NOx simulation in large-scale 3-D models. *Journal of Geophysical Research: Atmospheres*, *122*(5), 3141-3154.

López, J. A., Montanyà, J., van der Velde, O. A., Pineda, N., Salvador, A., Romero, D., ... & Taborda, J. (2019). Charge structure of two tropical thunderstorms in Colombia. *Journal of Geophysical Research: Atmospheres*, *124*(10), 5503-5515.

Lyons, W. A., Bruning, E. C., Warner, T. A., MacGorman, D. R., Edgington, S., Tillier, C., & Mlynarczyk, J. (2020). Megaflashes: Just how long can a lightning discharge get?. *Bulletin of the American Meteorological Society*, *101*(1), E73-E86.

Mach, D. M., Christian, H. J., Blakeslee, R. J., Boccippio, D. J., Goodman, S. J., & Boeck, W. L. (2007). Performance assessment of the optical transient detector and lightning imaging sensor. *Journal of Geophysical Research: Atmospheres*, *112*(D9).

Marshall, T. C., & Rust, W. D. (1991). Electric field soundings through thunderstorms. *Journal of Geophysical Research: Atmospheres*, *96*(D12), 22297-22306.

Marshall, T. C., Rust, W. D., Winn, W. P., & Gilbert, K. E. (1989). Electrical structure in two thunderstorm anvil clouds. *Journal of Geophysical Research: Atmospheres*, *94*(D2), 2171-2181.

Mansell, E. R., MacGorman, D. R., Ziegler, C. L., & Straka, J. M. (2005). Charge structure and lightning sensitivity in a simulated multicell thunderstorm. *Journal of Geophysical Research: Atmospheres*, *110*(D12).

769 Mecikalski, R. M., & Carey, L. D. (2018). Radar reflectivity and altitude distributions of
770 lightning as a function of IC, CG, and HY flashes: Implications for LNOx production.
771 *Journal of Geophysical Research: Atmospheres*, *123*(22), 12-796.
772 Peterson, M. (2019). Research applications for the Geostationary Lightning Mapper operational
773 lightning flash data product. *Journal of Geophysical Research: Atmospheres*, *124*(17-18),
774 10205-10231.
775 Peterson, M. (2021). Where are the most extraordinary lightning megaflashes in the Americas?.
776 *Bulletin of the American Meteorological Society*, *102*(3), E660-E671.
777 Peterson, M. (2022). FORTE Lightning Altitude Data, https://doi.org/10.7910/DVN/0ZWPTL,
778 Harvard Dataverse, DRAFT VERSION
779 Peterson, M., & Rudlosky, S. (2019). The time evolution of optical lightning flashes. *Journal of*
780 *Geophysical Research: Atmospheres*, *124*(1), 333-349.
781 Peterson, M., & Stano, G. (2021). The Hazards Posed by Mesoscale Lightning Megaflashes.
782 *Earth Interactions*, *25*(1), 46-56.
783 Peterson, M., Rudlosky, S., & Deierling, W. (2017a). The evolution and structure of extreme
784 optical lightning flashes. *Journal of Geophysical Research: Atmospheres*, *122*(24), 13-
785 370.
786 Peterson, M., Deierling, W., Liu, C., Mach, D., & Kalb, C. (2017b). The properties of optical
787 lightning flashes and the clouds they illuminate. *Journal of Geophysical Research:*
788 *Atmospheres*, *122*(1), 423-442.
789 Peterson, M., Rudlosky, S., & Deierling, W. (2018). Mapping the lateral development of
790 lightning flashes from orbit. *Journal of Geophysical Research: Atmospheres*, *123*(17),
791 9674-9687.

792 Peterson, M., Light, T. E., & Shao, X. M. (2021a). Combined Optical and Radio-Frequency
793 Measurements of a Lightning Megaflash by the FORTE Satellite. *Journal of Geophysical*
794 *Research: Atmospheres*, *126*(15), e2020JD034411.
795 Peterson, M., Light, T. E. L., & Shao, X.-M. (2021b). Combined optical and radio-frequency
796 perspectives on a hybrid Cloud-to-Ground lightning flash observed by the FORTE
797 satellite. *Journal of Geophysical Research: Atmospheres*, 126, e2020JD034152.
798 https://doi.org/10.1029/2020JD034152
799 Peterson, M., Mach, D., & Buechler, D. (2021c). A Global LIS/OTD Climatology of Lightning
800 Flash Extent Density. *Journal of Geophysical Research: Atmospheres*, *126*(8),
801 e2020JD033885.
802 Pickering, K. E., Wang, Y., Tao, W. K., Price, C., & Müller, J. F. (1998). Vertical distributions
803 of lightning NOx for use in regional and global chemical transport models. *Journal of*
804 *Geophysical Research: Atmospheres*, *103*(D23), 31203-31216.
805 Rakov, V. A., & Uman, M. A. (2003). *Lightning: physics and effects*. Cambridge university
806 press.
807 Reynolds, S. E., Brook, M., & Gourley, M. F. (1957). Thunderstorm charge separation. Journal
808 of Meteorology, 14(5), 163–178.
809 Rison, W., Thomas, R. J., Krehbiel, P. R., Hamlin, T., & Harlin, J. (1999). A GPS-based three-
810 dimensional lightning mapping system: Initial observations in central New Mexico.
811 *Geophysical research letters*, *26*(23), 3573-3576.
812 Saunders, C. P. R., & Peck, S. L. (1998). Laboratory studies of the influence of the rime
813 accretion rate on charge transfer during crystal/graupel collisions. *Journal of Geophysical*
814 *Research: Atmospheres*, *103*(D12), 13949-13956.

Saunders, C. P. R., Keith, W. D., & Mitzeva, R. P. (1991). The effect of liquid water on thunderstorm charging. *Journal of Geophysical Research: Atmospheres*, *96*(D6), 11007-11017.

Schuur, T. J., & Rutledge, S. A. (2000). Electrification of stratiform regions in mesoscale convective systems. Part I: An observational comparison of symmetric and asymmetric MCSs. *Journal of the atmospheric sciences*, *57*(13), 1961-1982.

Seiler, W., & Crutzen, P. J. (1980). Estimates of gross and net fluxes of carbon between the biosphere and the atmosphere from biomass burning. *Climatic change*, *2*(3), 207-247.

Shao, X. M., & Krehbiel, P. R. (1996). The spatial and temporal development of intracloud lightning. *Journal of Geophysical Research: Atmospheres*, *101*(D21), 26641-26668.

Simpson, G. C., & Scrase, F. J. (1937). The distribution of electricity in thunderclouds. *Proceedings of the Royal Society of London. Series A-Mathematical and Physical Sciences*, *161*(906), 309-352.

Smith, D. A., Heavner, M. J., Jacobson, A. R., Shao, X. M., Massey, R. S., Sheldon, R. J., & Wiens, K. C. (2004). A method for determining intracloud lightning and ionospheric heights from VLF/LF electric field records. *Radio Science*, *39*(1), 1-11.

Stolzenburg, M., Rust, W. D., Smull, B. F., & Marshall, T. C. (1998). Electrical structure in thunderstorm convective regions: 1. Mesoscale convective systems. *Journal of Geophysical Research: Atmospheres*, *103*(D12), 14059-14078.

Suszcynsky, D. M., & Heavner, M. J. (2003). Narrow bipolar events as indicators of thunderstorm convective strength. *Geophysical research letters*, *30*(17).

Suszcynsky, D. M., Kirkland, M. W., Jacobson, A. R., Franz, R. C., Knox, S. O., Guillen, J. L. L., & Green, J. L. (2000). FORTE observations of simultaneous VHF and optical

838 emissions from lightning: Basic phenomenology. *Journal of Geophysical Research:*
839 *Atmospheres*, *105*(D2), 2191-2201.
840 Suszcynsky, D. M., Light, T. E., Davis, S., Green, J. L., Guillen, J. L. L., & Myre, W. (2001).
841 Coordinated observations of optical lightning from space using the FORTE photodiode
842 detector and CCD imager. *Journal of Geophysical Research: Atmospheres*, *106*(D16),
843 17897-17906.
844 Takahashi, T. (1978). Riming electrification as a charge generation mechanism in thunderstorms.
845 *Journal of Atmospheric Sciences*, *35*(8), 1536-1548.
846 Takahashi, T., & Miyawaki, K. (2002). Reexamination of riming electrification in a wind tunnel.
847 *Journal of the Atmospheric Sciences*, *59*(5), 1018-1025.
848 Thomas, R. J., Krehbiel, P. R., Rison, W., Hamlin, T., Boccippio, D. J., Goodman, S. J., &
849 Christian, H. J. (2000). Comparison of ground-based 3-dimensional lightning mapping
850 observations with satellite-based LIS observations in Oklahoma. *Geophysical research*
851 *letters*, *27*(12), 1703-1706.
852 Thomas, R. J., Krehbiel, P. R., Rison, W., Hunyady, S. J., Winn, W. P., Hamlin, T., & Harlin, J.
853 (2004). Accuracy of the lightning mapping array. *Journal of Geophysical Research:*
854 *Atmospheres*, *109*(D14).
855 Tie, X., Zhang, R., Brasseur, G., & Lei, W. (2002). Global NOx production by lightning. *Journal*
856 *of Atmospheric Chemistry*, *43*(1), 61-74.
857 Williams, E. R. (1989). The tripole structure of thunderstorms. *Journal of Geophysical*
858 *Research: Atmospheres*, *94*(D11), 13151-13167.
859 Williams, E. (2018). Lightning activity in winter storms: A meteorological and cloud
860 microphysical perspective. *IEEJ Transactions on Power and Energy*, *138*(5), 364-373.

Wilson, C. T. R. (1920). III. Investigations on lightning discharges and on the electric field of thunderstorms. *Philosophical Transactions of the Royal Society of London. Series A, Containing Papers of a Mathematical or Physical Character*, *221*(582-593), 73-115.

Wu, T., Wang, D., Huang, H., & Takagi, N. (2021). The strongest negative lightning strokes in winter thunderstorms in Japan. *Geophysical Research Letters*, *48*(21), e2021GL095525.

Yamamoto, M. K., Higuchi, A., & Nakamura, K. (2006). Vertical and horizontal structure of winter precipitation systems over the western Pacific around Japan using TRMM data. *Journal of Geophysical Research: Atmospheres*, *111*(D13).

Zheng, D., Wang, D., Zhang, Y., Wu, T., & Takagi, N. (2019). Charge regions indicated by LMA lightning flashes in Hokuriku's winter thunderstorms. *Journal of Geophysical Research: Atmospheres*, *124*(13), 7179-7206.

Table 1. Variations in RF pulse feature counts after successively applying each filter. The final 2 filters are only applied for the analyses in Section 3.3 and the Supporting Information (SI).

	All Pulses	TIPPs	TIPPS w/LLS Coincidence
No Filters	3,089,812	1,096,885	380,347
Valid TEC	2,694,726	1,006,466	330,302
Centered in Record	2,437,408	907,083	300,214
Isolated in Time	1,796,217	695,146	202,062
1 Active LLS Area	-	-	152,955
1 Active LLS Flash	-	-	130,261

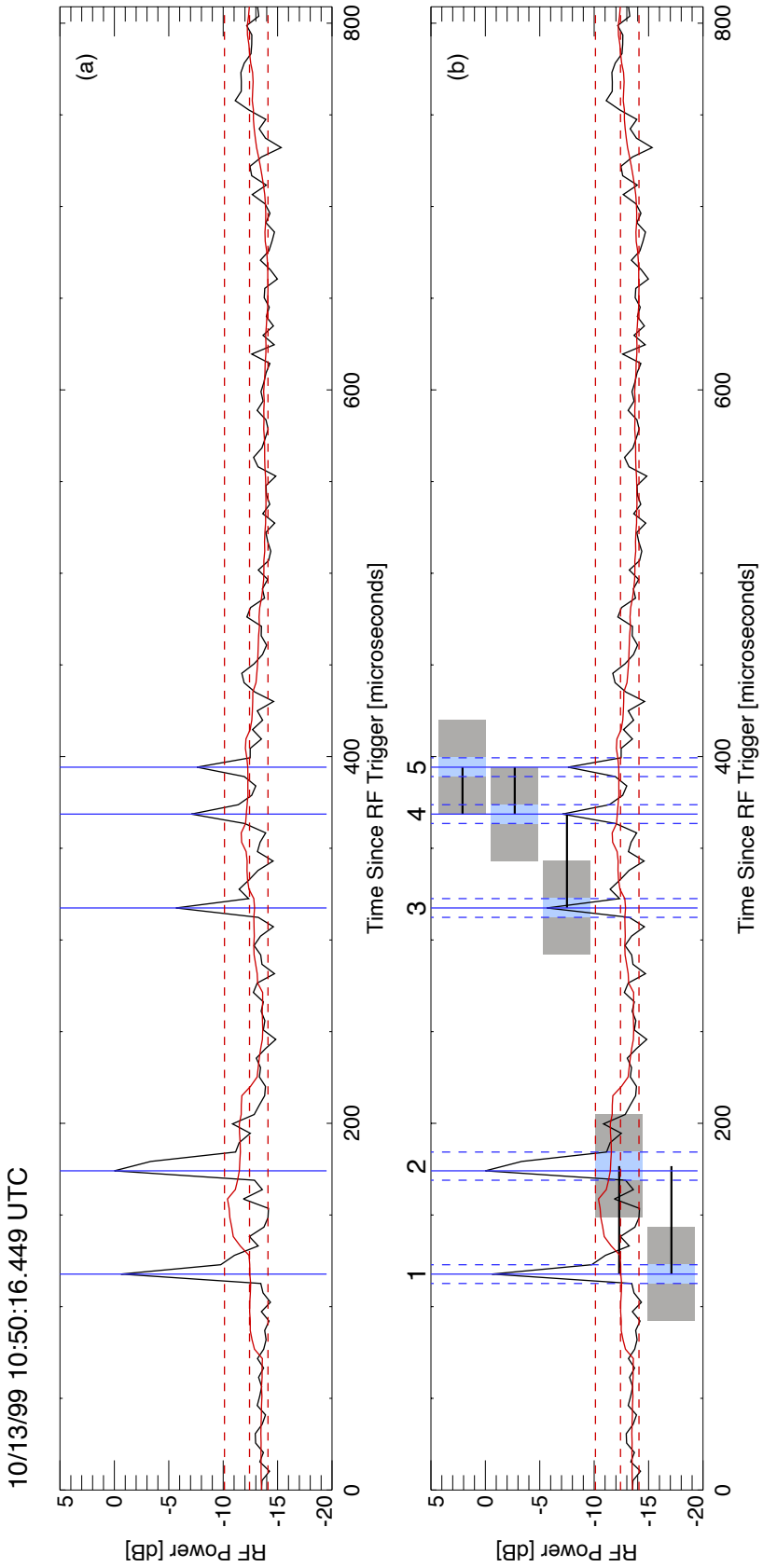

Figure 1. Example RF event record with multiple identified pulses. Peak (solid blue vertical lines) and pulse (blue bars between dashed blue lines) features are identified from contiguous regions of the original power timeseries (black curve) that are 3 standard deviations (horizontal dashed lines) above the minimum of the smoothed timeseries (red curve), as described in text. Pulse windows used to compute their properties (grey bars) and links between pairs of impulsive events (horizontal black lines) are also shown.

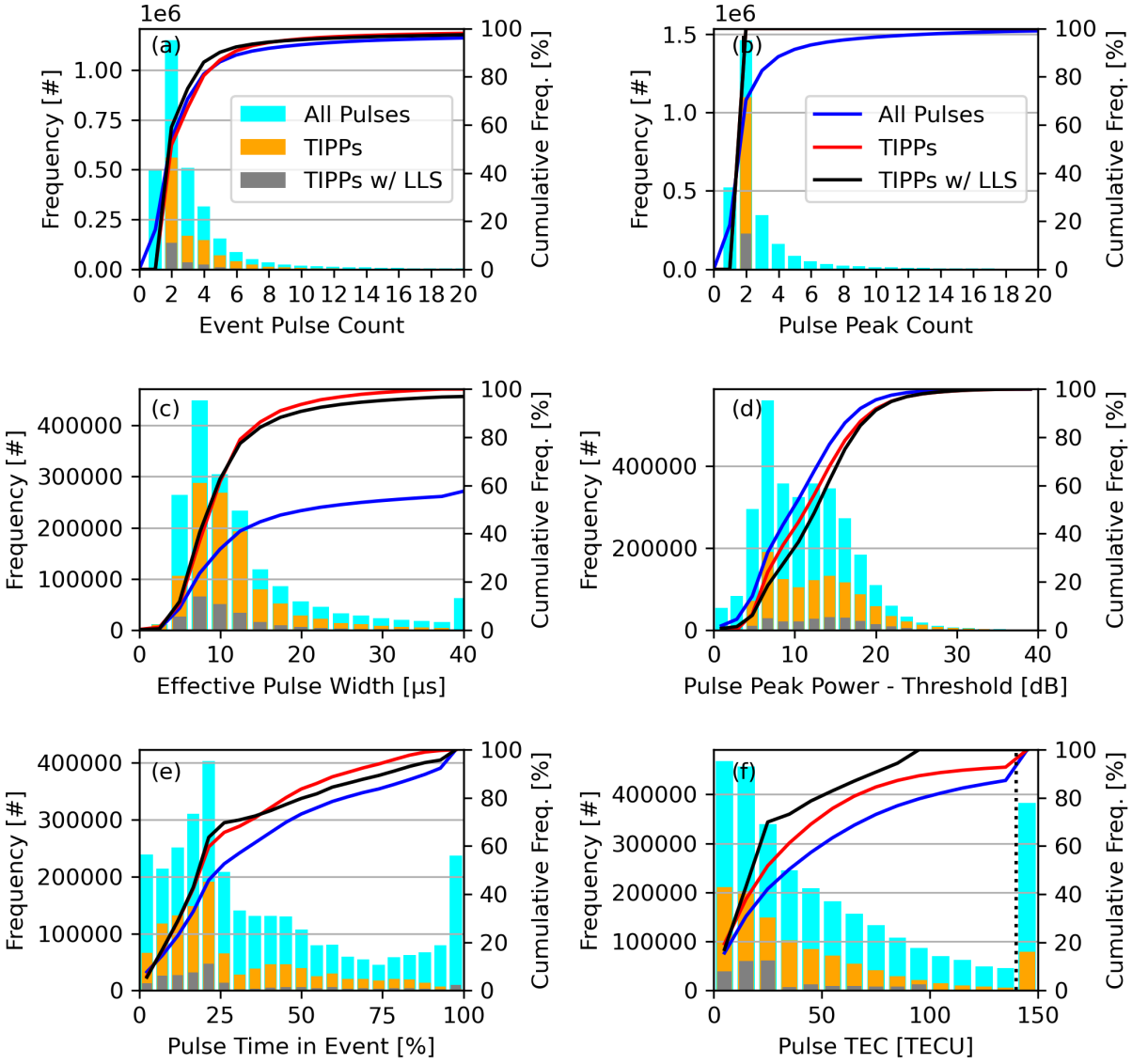

Figure 2. Histograms and cumulative distributions of (a) the number of pulses per event, (b) the number of peaks per pulse, (c) the effective pulse with, (d) the peak power above the threshold, (e) the time of the pulse in the event record, and (f) the TEC experienced by the pulse reported by the dechirping algorithm. Separate distributions are shown for all pulses, TIPPs, and TIPPs that also have LLS coincidence at the flash level.

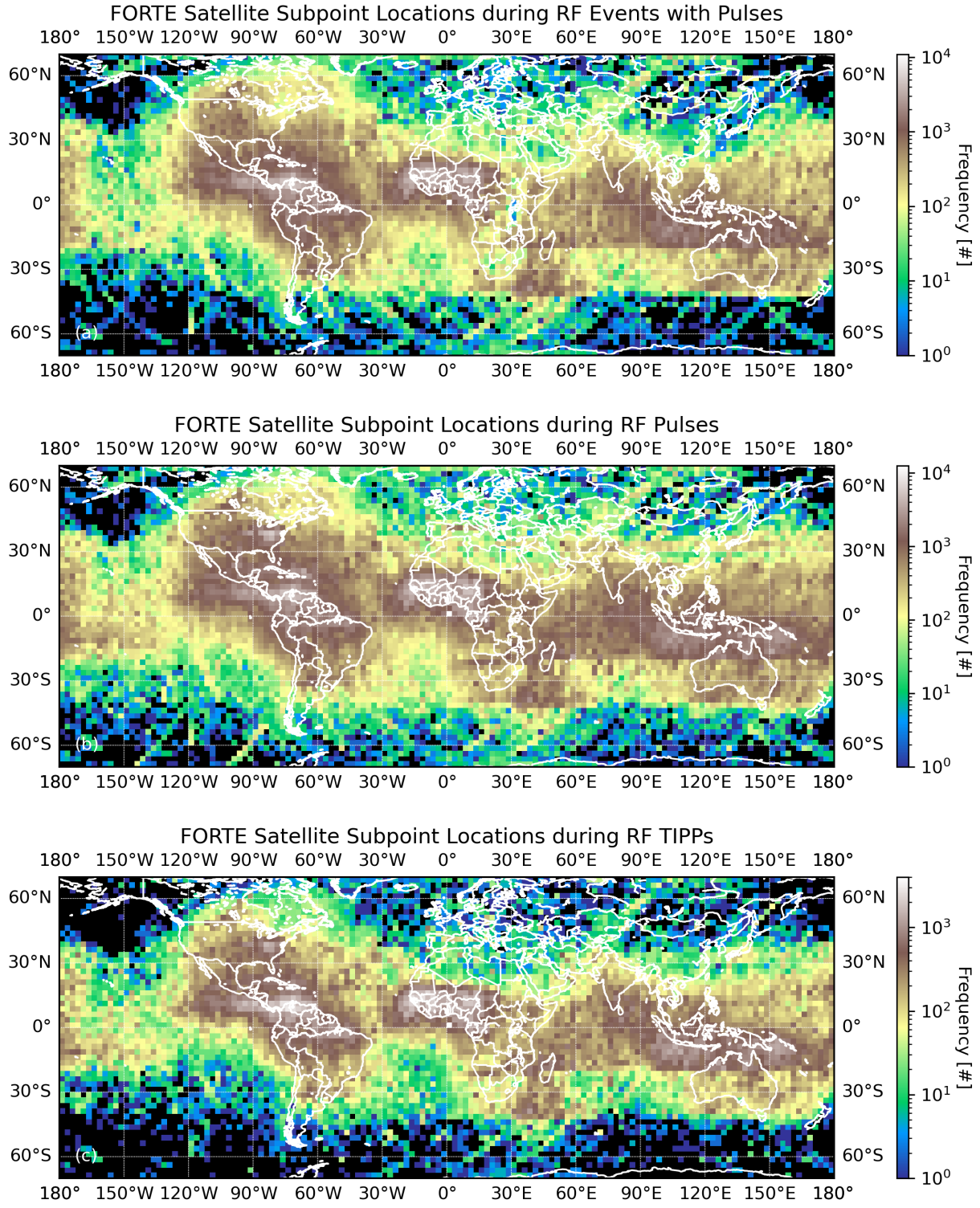

Figure 3. Global distributions of the FORTE satellite subpoint position during (a) RF events containing pulse features, (b) RF pulse features, and (c) RF TIPPs.

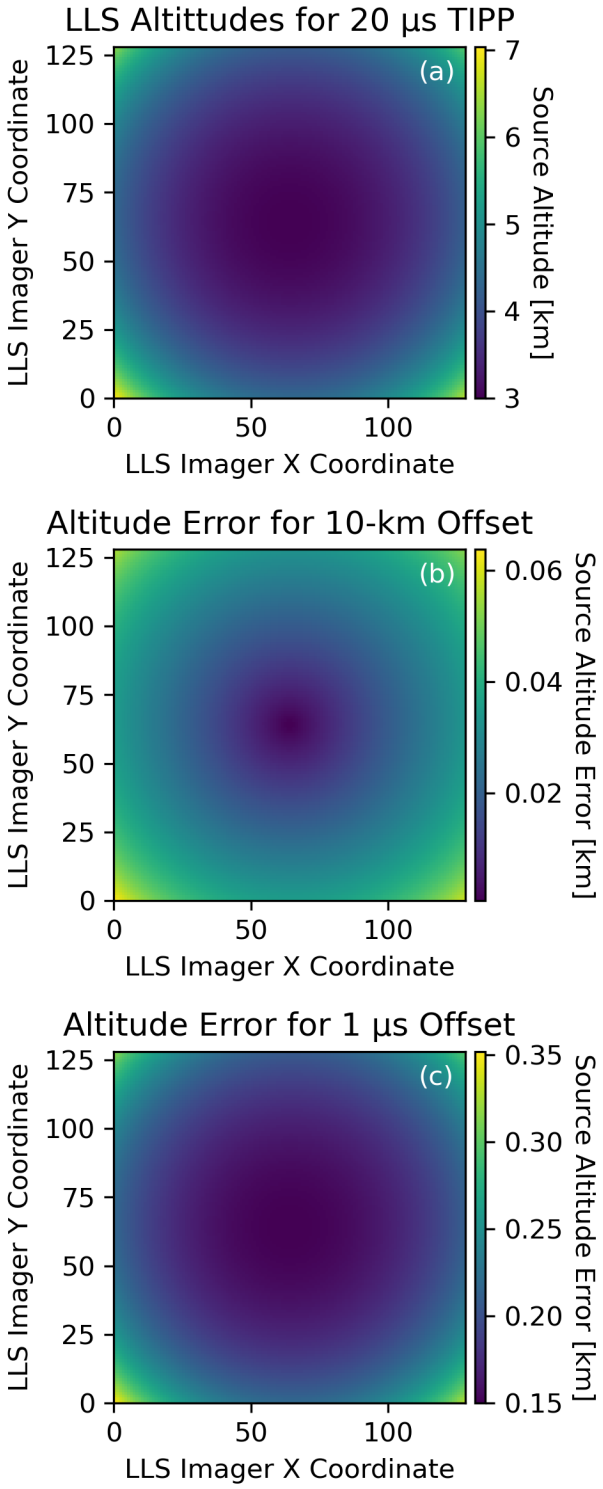

Figure 4. Distributions of altitude (a) and altitude error (b-c) for a TIPP with a 20 microsecond intra-pulse time interval located at each LLS imager pixel. (b) The altitude error from the detected VHF source being displaced 10 km radially outward from its true location. (c) The altitude error from the intra-pulse time interval being off by 1 microsecond.

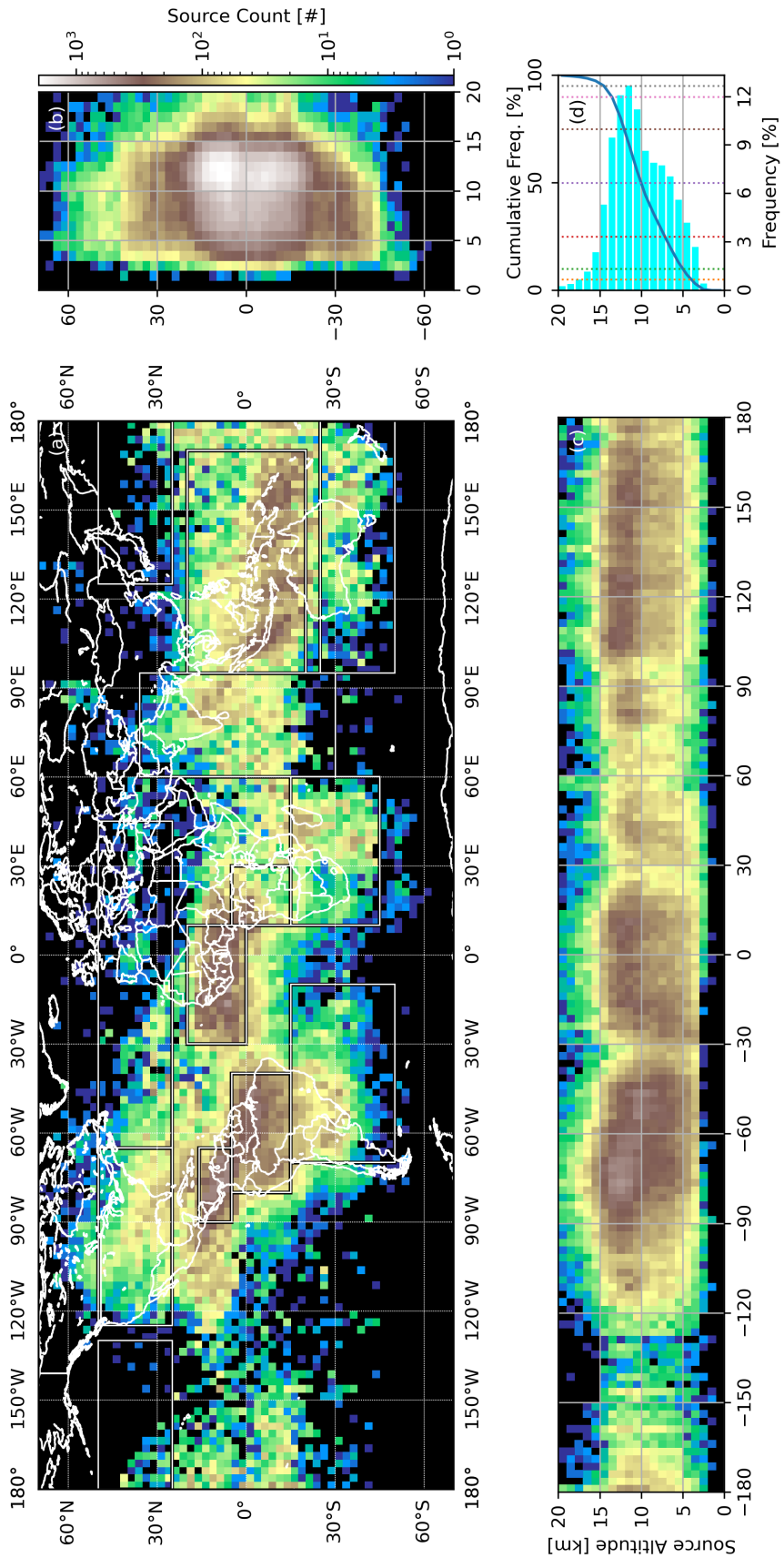

Figure 5. Distributions of LLS-coincident VHF sources. (a) Geographic distribution of VHF sources with regions of interest boxed. (b) Latitude-altitude source distribution. (c) Longitude-altitude distortion. (d) Global source altitude histogram (bars) and cumulative distribution (solid line).

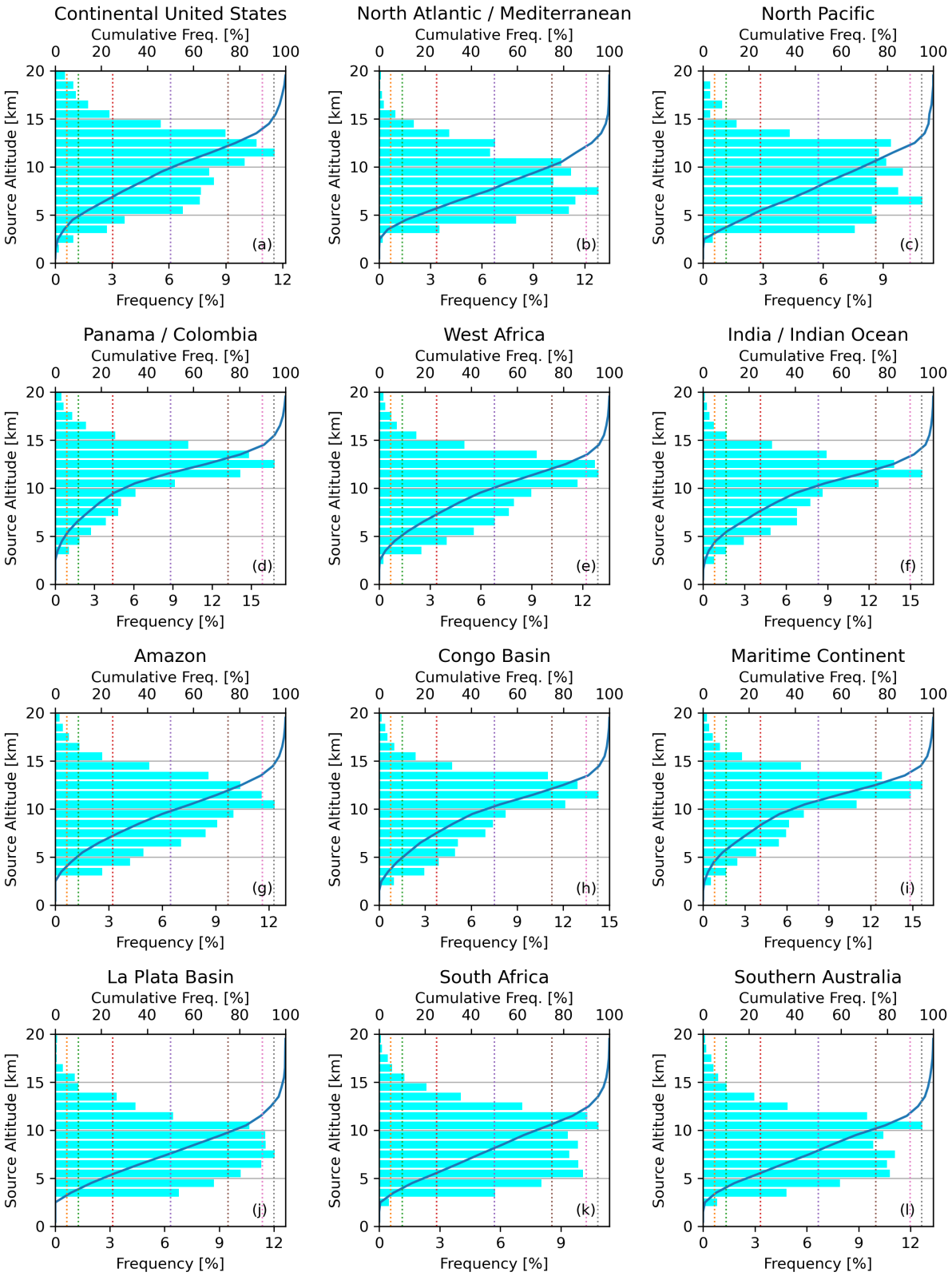

Figure 6. VHF source altitude profile for the regions boxed in Figure 5 organized by longitude (columns) and latitude (rows).

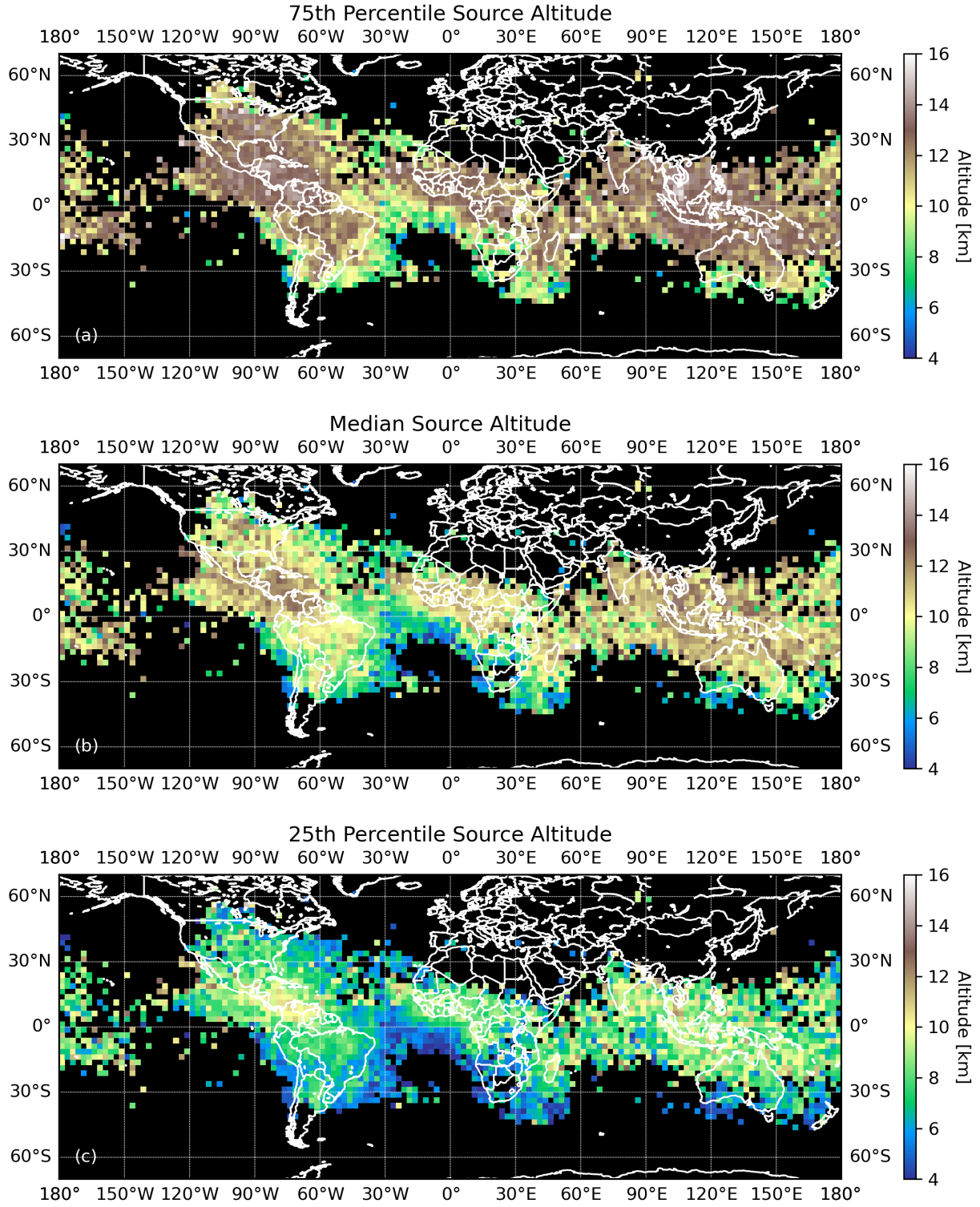

Figure 7. Global maps of (a) 75th percentile, (b) median, and (c) 25th percentile source altitudes.

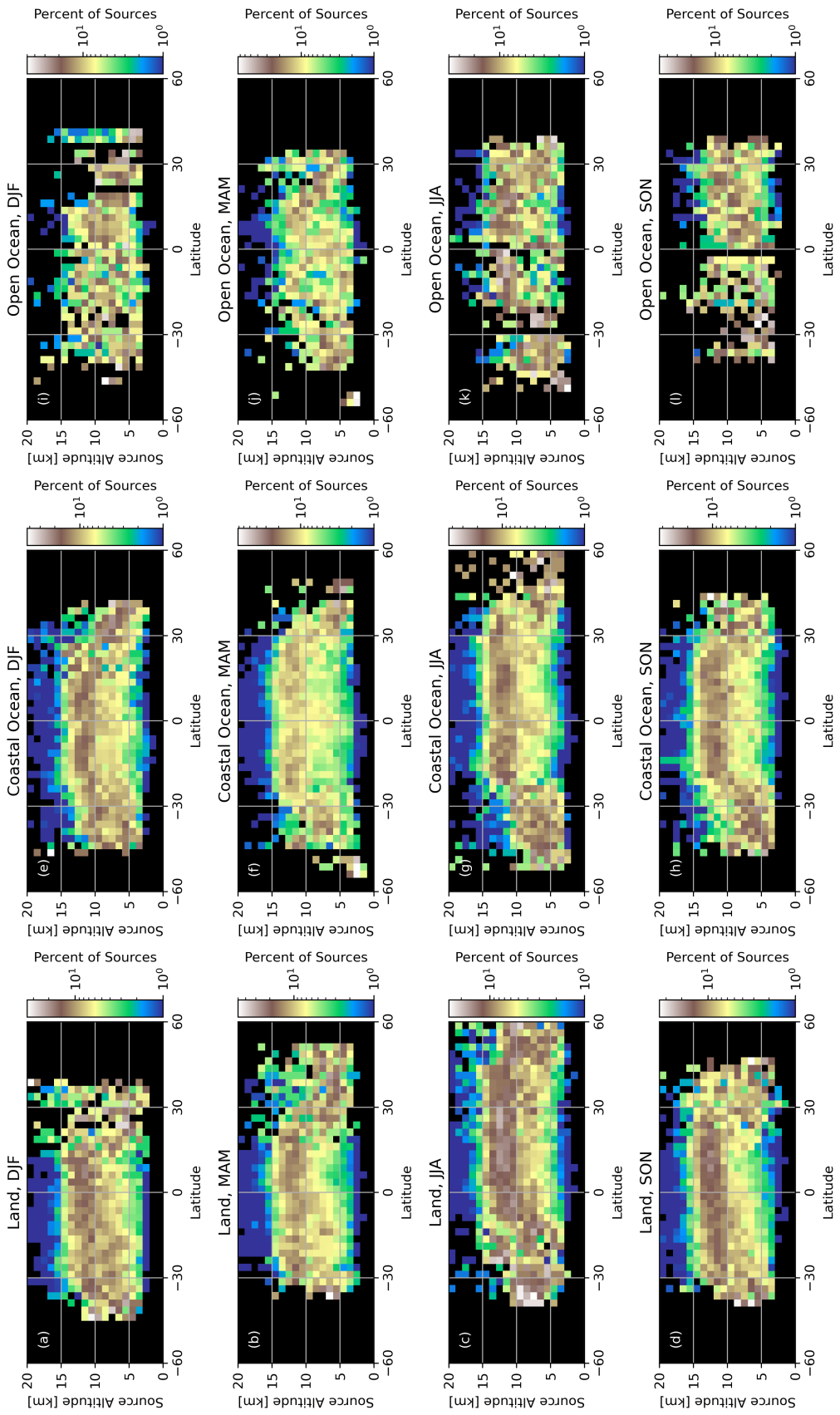

Figure 8. Latitude-altitude distributions of VHF sources detected over land (left), the coastal ocean (center), and the open ocean (right) during December-February (top row), March-May (second row), June – August (third row), and September – November (bottom row).

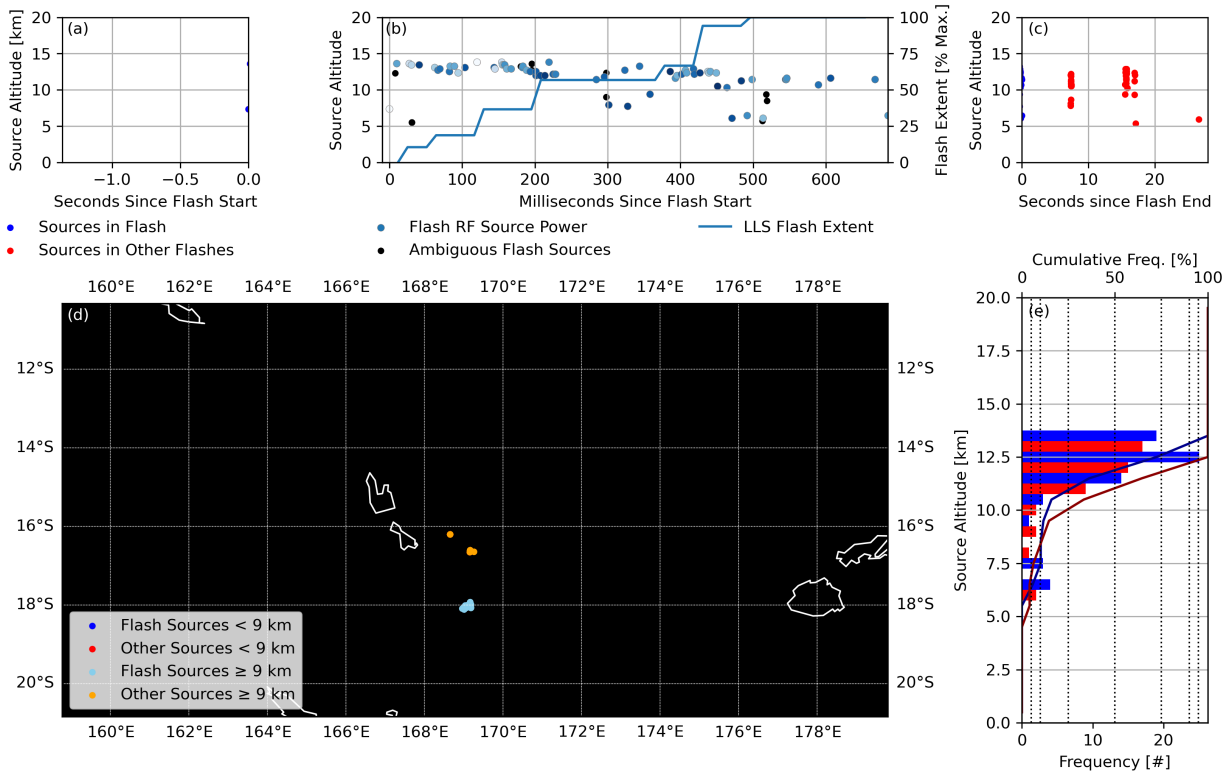

Figure 9. Altitude timeseries of source altitudes (a) before, (b) during, and (c) after an LLS flash of interest. Sources that were part of the flash are shown in blue, while sources in other flashes are shown in red. The locations of these sources are mapped in (d), and their vertical profiles are shown in (e). The blue color scale in (b) denotes RF power from minimum (dark blue) to maximum (white). Sources with ambiguous TIPP links are denoted with black in (b). Sources in (d) are shaded according to altitude.

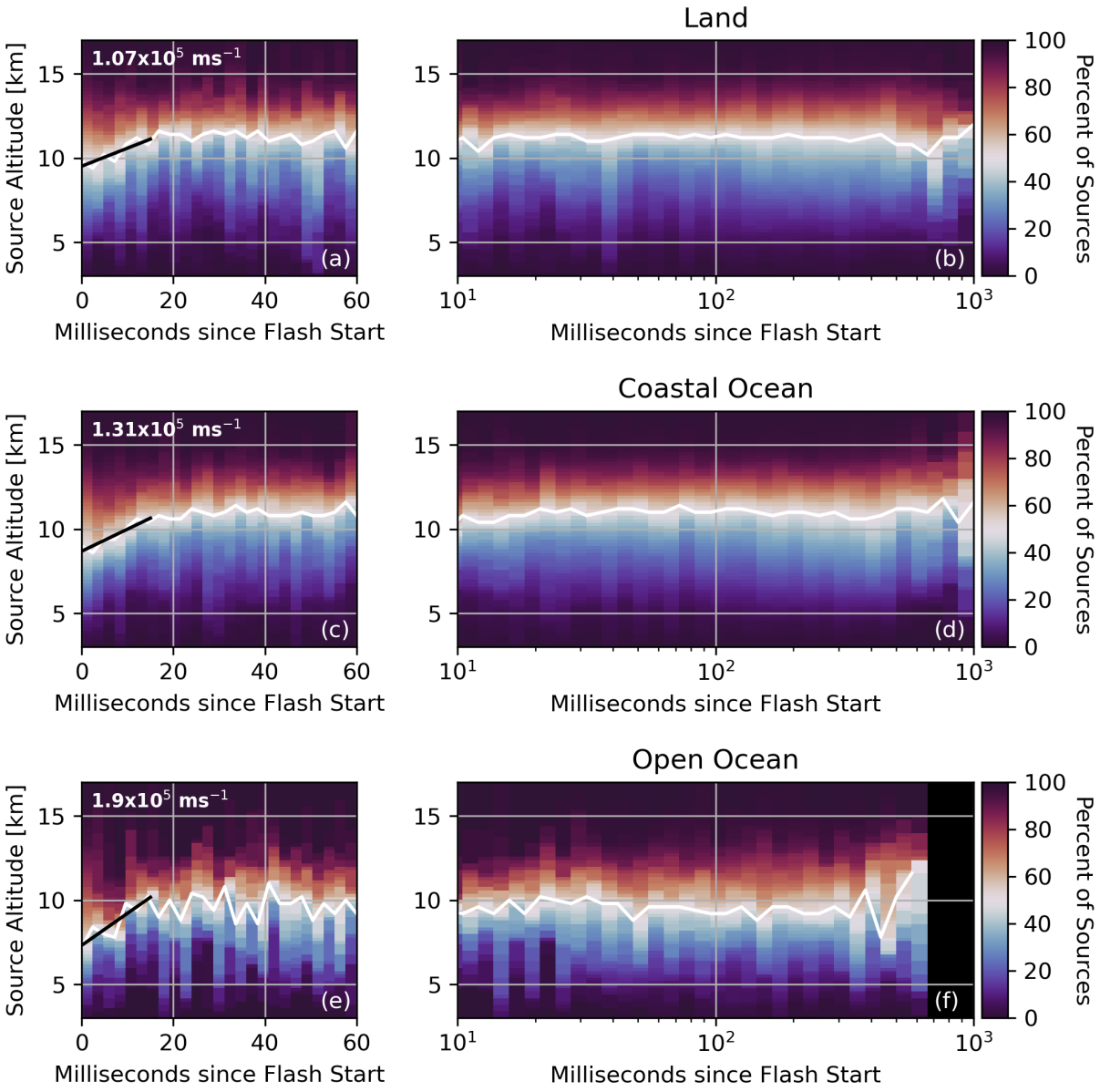

Figure 10. Cumulative distributions of source attitude at each point over the duration of land (top row), coastal ocean (middle row) and open ocean (bottom) flashes. Early activity in the flash is shown with linear temporal bins in the left column, while the full flash duration is shown with logarithmic temporal bins in the right column. Linear fits to the median altitude in the first 15 ms of the flashes are shown with black lines whose slope approximates typical vertical propagation speeds (listed at the top of the plot) for negative leaders in each region.

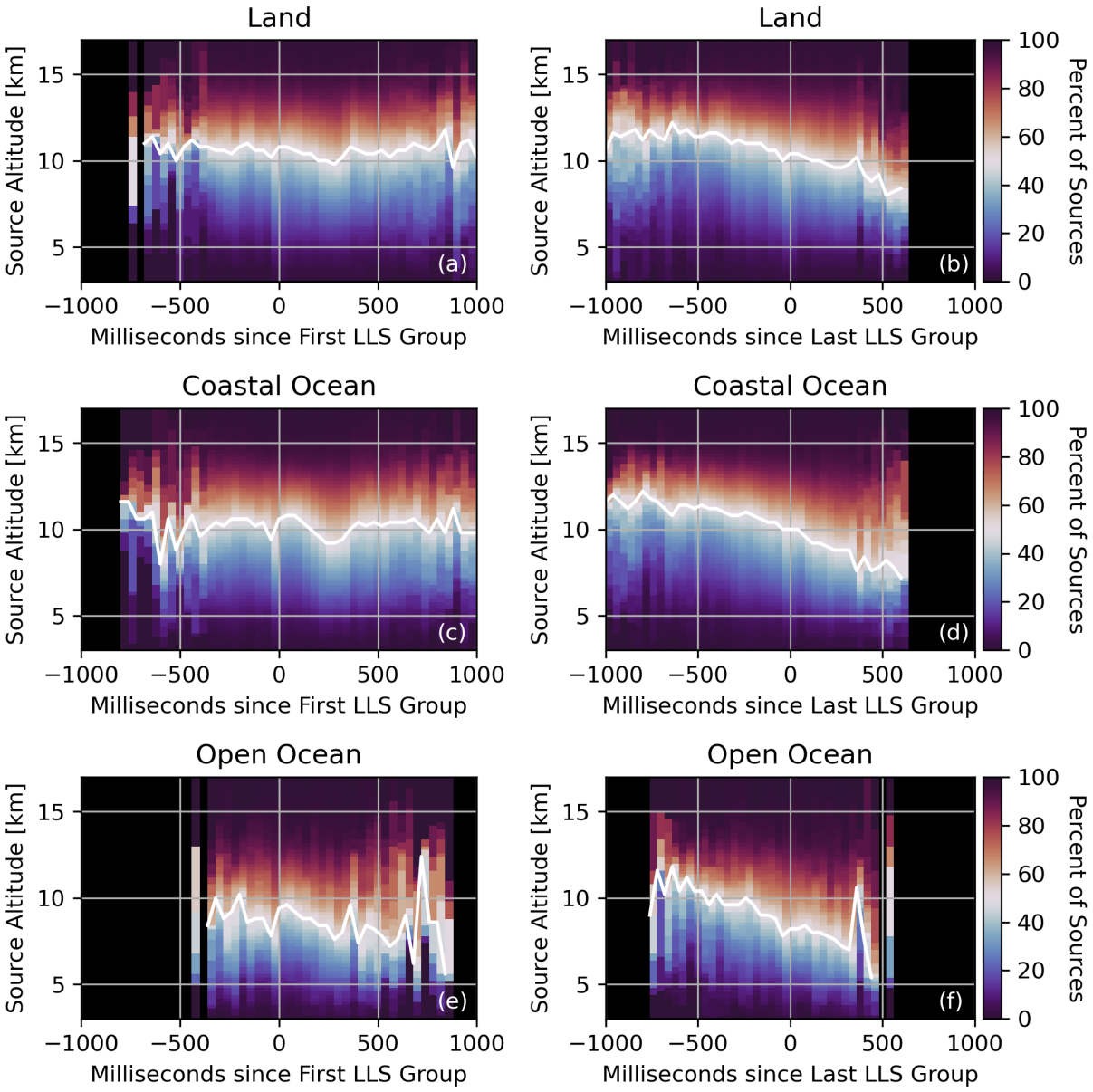

Figure 11. Cumulative distributions of source attitude at each point relative to the first LLS group in the flash (left) and the last LLS group in the flash (right). Separate distributions are shown for land (top), the coastal ocean (middle) and open ocean (bottom).

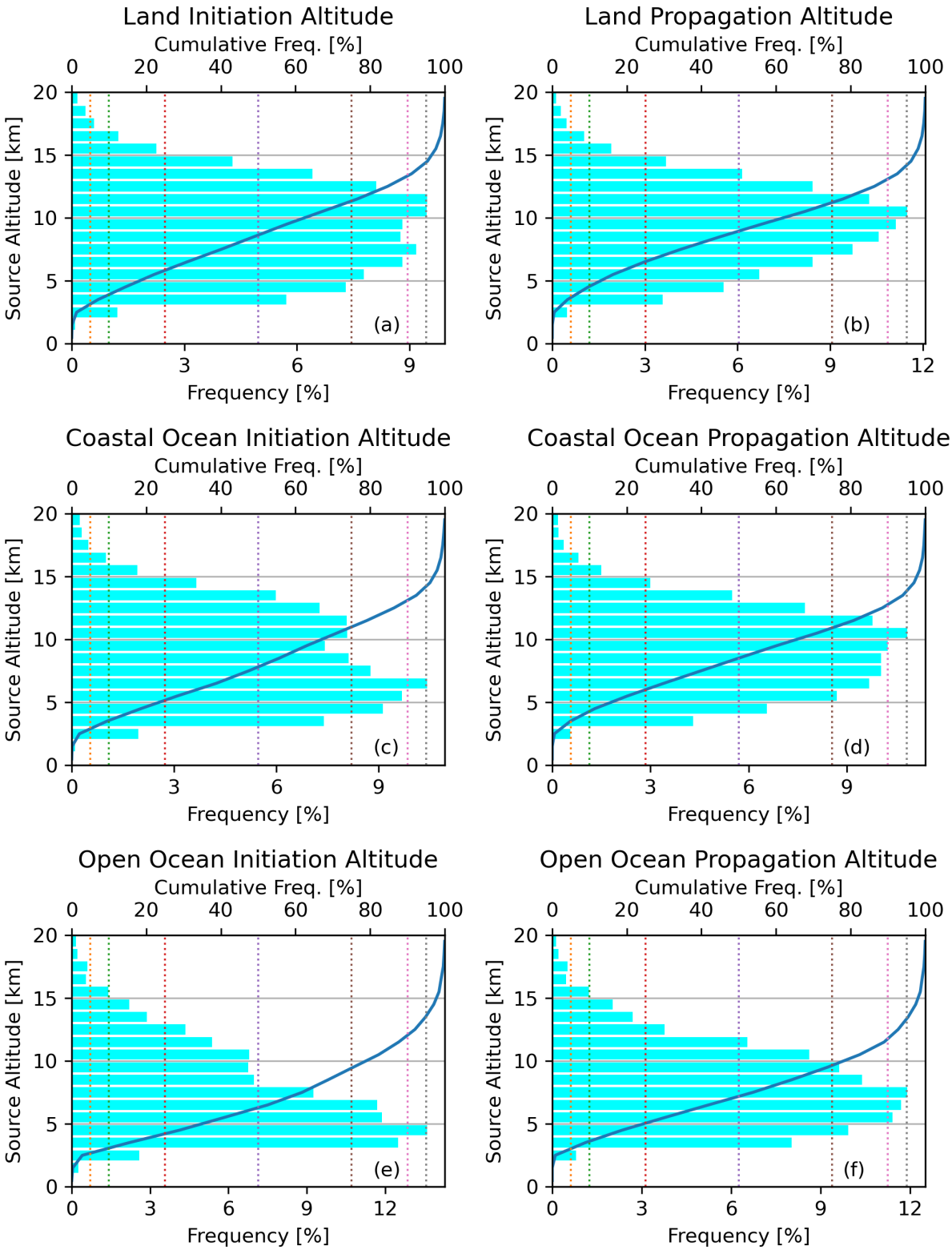

960
961 **Figure 12.** Profiles of flash initiation altitude (left column) and propagation altitude (right
962 column) for flashes over land (top row), the coastal ocean (middle row), and the open ocean
963 (bottom row).